



**HAL**  
open science

# Twinning and partial melting as early weakening processes in plagioclase at high pressure: insights from Holsnøy (Scandinavian Caledonides, Norway)

Marie Baïssset, Loïc Labrousse, Philippe Yamato, Alexandre Schubnel

► **To cite this version:**

Marie Baïssset, Loïc Labrousse, Philippe Yamato, Alexandre Schubnel. Twinning and partial melting as early weakening processes in plagioclase at high pressure: insights from Holsnøy (Scandinavian Caledonides, Norway). *Contributions to Mineralogy and Petrology*, 2023, 178, pp.19. 10.1007/s00410-023-01998-x . insu-04029578

**HAL Id: insu-04029578**

**<https://insu.hal.science/insu-04029578>**

Submitted on 15 Mar 2023

**HAL** is a multi-disciplinary open access archive for the deposit and dissemination of scientific research documents, whether they are published or not. The documents may come from teaching and research institutions in France or abroad, or from public or private research centers.

L'archive ouverte pluridisciplinaire **HAL**, est destinée au dépôt et à la diffusion de documents scientifiques de niveau recherche, publiés ou non, émanant des établissements d'enseignement et de recherche français ou étrangers, des laboratoires publics ou privés.

1 **Twinning and partial melting as early weakening processes in**  
2 **plagioclase at high pressure: insights from Holsnøy (Scandinavian**  
3 **Caledonides, Norway)**

4 **Marie Bâisset<sup>1\*</sup>, Loïc Labrousse<sup>1</sup>, Philippe Yamato<sup>2,3</sup>, and Alexandre Schubnel<sup>4</sup>**

5 *<sup>1</sup>Sorbonne Université, CNRS-INSU, Institut des Sciences de la Terre Paris, ITeP, UMR7193,*  
6 *France*

7 *<sup>2</sup>Univ Rennes, CNRS, Géosciences Rennes - UMR 6118, F-35000 Rennes, France*

8 *<sup>3</sup>Institut Universitaire de France, Paris, France*

9 *<sup>4</sup>Laboratoire de Géologie de l'ENS - PSL University - UMR8538 du CNRS, France*

10 \*Corresponding author: Marie Bâisset, marie.baisset.pro@gmail.com (ORCID ID: 0000-0001-  
11 5611-5470)

12 **Statements and Declarations**

13 **Competing Interests**

14 There is no conflict of interest.

15 **Data availability**

16 The data underlying this article will be shared on request to the corresponding author.

17 **Acknowledgements**

18 We thank E. Bras for his help in sampling and mapping in the field. M.B. thanks D.  
19 Deldicque and O. Boudouma for the EBSD analyses performed at ENS Paris and  
20 Sorbonne Université, respectively. We thank W. Cao, S. Schorn and an anonymous  
21 reviewer for their constructive suggestions that truly helped improve that manuscript. J.  
22 Hermann and L. Menegon are especially thank for fruitful discussions on petrological

23 aspects around melting and thermodynamic equilibrium, and mechanical considerations,  
24 respectively. A.S. acknowledges the European Research Council grant REALISM (2016-  
25 grant 681346). P.Y. acknowledges the Institut Universitaire de France for financial  
26 support.

## 27 **Abstract**

28 Eclogitization reactions of plagioclase-bearing rocks in water-limited environments  
29 are often incomplete. In such domains, metamorphism and strain localization interact,  
30 yielding complex strain-transformation patterns in the field. This is the case in the granulite  
31 facies anorthosites of Holsnøy, where partial eclogitization proceeds along digitations in  
32 the least strained domains. These areas are among the rare examples of preserved early  
33 eclogitization textures. The aim of this study is to assess the mechanical alteration induced  
34 by plagioclase breakdown reactions, through a detailed petrological study of the very first  
35 increments of the eclogitization process, expected to be preserved at the tip of a digitation  
36 in an apparently undeformed granulite block. We show that (i) the zoisite-forming reaction  
37 within plagioclase grains occurs unbalanced and initiates mechanical twinning, and  
38 subgrains individualization, and (ii) kyanite-analcime association at plagioclase grain  
39 boundaries gives evidence of partial melting, which might have affected the rock near the  
40 peak  $P$ – $T$  conditions in response to early water infiltration. This transient partial melting  
41 stage results in the re-crystallization of  $\mu\text{m}$ -scale plagioclase grains. Intra-grain and grain  
42 boundary transformations therefore induce an effective grain size reduction. It constitutes  
43 an alteration of the overall aggregate properties of the burying continental rocks, prior to  
44 any significant deformation, at potentially low differential stress. Partially transformed  
45 granulites are eventually weaker than initial granulites and are prone to later strain  
46 localization.

47 **Keywords:** eclogitization process; reaction-induced weakening; partial melting;  
48 plagioclase mechanical twinning; grain size reduction

## 49 1. Introduction

50 Eclogitization is known to trigger important changes in mechanical properties of  
51 rocks (i.e., strength and density), and is therefore considered as a key process for the  
52 dynamics of convergence zones at short time scales (seismicity – [Austrheim and Boundy](#)  
53 [1994](#); [Lund and Austrheim 2003](#); [Hacker et al. 2003](#)) as well as on the long-term (plate  
54 tectonics – [Kirby et al. 1996](#); [Jung et al. 2004](#); [Jackson et al. 2004](#); [Hetényi et al. 2021](#)).  
55 Concomitance between eclogitization reactions and deformation localization in ductile  
56 shear-zones or in pseudotachylytes has been extensively described ([Austrheim and](#)  
57 [Boundy 1994](#); [Früh-Green 1994](#); [Lund and Austrheim 2003](#); [John and Schenk, 2006](#);  
58 [Steltenpohl et al. 2006](#); [Scambelluri et al. 2017](#)). Although eclogitization is acknowledged  
59 as a trigger for changes in the effective strength of rocks, how eclogitization reactions  
60 induce these rheological changes is still under investigation today. Indeed, eclogitization  
61 of rocks consists in a set of reactions of variable kinetics, that successively take place with  
62 increasing pressure and lead to the eventual formation of garnet and omphacite as index  
63 phases, but also secondary phases depending on the chemical system of the rock. These  
64 reactions can be responsible for grain size reduction, for the release or consumption of  
65 fluids, and can also lead to the nucleation of newly formed weaker or stronger phases, all  
66 these processes being able to strongly affect the mechanical properties of the rock.  
67 However, as several progressive transformations are involved in the eclogitization  
68 process, the first reactions may generate transient phases and textures later obliterated  
69 by the subsequent reactions. In particular, within deformed zones where reactions usually  
70 reached completion, these transient steps are not visible anymore. It is therefore crucial  
71 to study undeformed and partially transformed zones where the first steps of mineral  
72 breakdown may have been preserved ([Wayte et al. 1989](#)). It is indeed possible that these  
73 first reaction steps play a major role in the ultimate localization of deformation ([Brodie and](#)  
74 [Rutter 1985](#)).

75 Eclogitization of the continental lower crust constitutes a perfect case study for  
76 depicting these first reaction stages, due to the low reactivity of dry plagioclase, one of its  
77 main rock-forming mineral ([Wain et al. 2001](#); [John and Schenk 2003](#); [Young and](#)  
78 [Kylander-Clark 2015](#); [Schorn and Diener 2017](#); [Shi et al. 2018](#); [Incel et al. 2019](#)). The

79 breakdown of this phase with increasing pressure involves two chemical systems that  
80 present contrasted stoichiometries ([Holland 1980](#); [Goldsmith 1982](#)) and decoupled  
81 kinetics due to slow interdiffusion of NaSi and CaAl ([Wayte et al. 1989](#)): (1) the hydrated  
82 Ca-system (zoisite formation from the reaction anorthite + H<sub>2</sub>O = zoisite + kyanite +  
83 quartz), and (2) the Na-system (jadeite formation from reaction albite = jadeite + quartz).  
84 If reaction (2) has often been considered of major importance in the eclogitization process  
85 and its mechanical consequences ([Shi et al. 2018](#); [Incel et al. 2019](#)), reaction (1) that  
86 initiates earlier along the prograde *P–T* path is still an underrated transformation. For  
87 instance, the crystallization kinetics and mechanical properties of epidote are still poorly  
88 known, although being one of the most ubiquitous minerals of metamorphism. However,  
89 because fluids are involved in its balance, reaction kinetics can be very fast as soon as  
90 fluids enter the system ([Wayte et al. 1989](#); [Rubie 1998](#); [Pattison et al. 2011](#)). This reaction  
91 is also characterized by a sensible volume change (~15%). It is therefore expected to  
92 generate fast changes of the state of stress inside the grains themselves, then  
93 mechanically destabilizing the rock at an early stage ([Stünitz and Tullis 2001](#)).

94         The island of Holsnøy (Scandinavian Caledonides) is ideal for studying the initial  
95 steps of plagioclase breakdown at high pressure, because initial granulite is only partially  
96 transformed (20 – 30% - [Boundy et al. 1992](#); [Putnis et al. 2017](#)). Zones of ongoing  
97 eclogitization of the granulite have been described and mapped ([Boundy et al. 1992](#)) in  
98 shear-zones ([Austrheim and Griffin 1985](#); [Kaatz et al. 2021](#); [Bras et al. 2021](#)), in  
99 pseudotachylytes and their damage zones ([Austrheim and Boundy 1994](#); [Petley-Ragan  
100 et al. 2018, 2019](#)), as well as in undeformed haloes spreading around a central vein, or in  
101 the form of diffuse patches (so-called eclogitic fingers – [Jamtveit et al. 2000](#); [Zertani et al.  
102 2019](#); [Putnis et al. 2021](#)).

103         In order to discuss the potential importance of early plagioclase breakdown on the  
104 mechanical behavior of its host-rock, we here present a detailed petrological analysis of  
105 the first steps of the breakdown processes affecting plagioclase grains at their boundaries  
106 as well as at their interior, through a transect into the tip of an eclogite finger. Through the  
107 study of plagioclase crystallographic orientation patterns around newly formed zoisite, we  
108 elaborate on the stresses recorded within the partially reacted plagioclase grains that can

109 be accommodated by the activation of twin systems although the granulite remains  
110 macroscopically undeformed. At plagioclase-plagioclase grain boundaries, transient  
111 products formed after plagioclase breakdown have been identified, such as kyanite-  
112 analcime-bearing associations that may result from crystallization after a melt. We use  
113 thermodynamic modelling to state that partial melting is possible at pressure and  
114 temperature ( $P$ - $T$ ) conditions close to the one acknowledged for Holsnøy rocks.  
115 Eventually, we elaborate on the importance of these initial stages of reaction and how  
116 they possibly contribute to mechanical alteration of the plagioclase matrix (grain size  
117 reduction, melt production) even before strain localization.

## 118 **2. Geological setting and sampling strategy**

### 119 **2.1 Geological context**

120 The area studied here is situated in the island of Holsnøy, Bergen Arcs, Western Norway,  
121 and is mostly composed of anorthosites and gabbros that underwent granulite facies  
122 metamorphism 930 Ma ago, during the Grenvillian orogeny ([Bingen et al. 2001](#)). The  
123 Bergen Arcs (inset Fig. 1a) have been formed by the nappe stacking of different units,  
124 which accretion results from the collision between Baltica and Laurentia during the  
125 Caledonian orogeny ([Roberts 2003](#)). The island of Holsnøy exposure belongs to the  
126 Lindås nappe ([Andersen et al. 1991](#)), composed of rocks that underwent high-pressure  
127 metamorphism during the collisional Scandian phase at 430 Ma ([Austrheim 1991](#); [Kühn  
128 et al. 2002](#), [Bingen et al. 2004](#); [Glodny et al. 2008](#); [Jamtveit et al. 2019](#)), and correlated  
129 to the Dalsford nappe in the Western Gneiss Complex, and the Jotun nappe within the  
130 Scandian nappe pile inland ([Andersen et al. 2012](#), [Jakob et al. 2022](#)). This  
131 tectonostratigraphic complex has been attributed to the distal part of the Baltica margin  
132 (the Jotun microcontinent, [Andersen et al. 2022](#)) imbricated within the Scandian wedge  
133 and then dilacerated during the late orogenic Caledonian extension.

134 Grenvillian granulite facies pervasive metamorphism occurred at temperatures of 800–  
135 850°C and pressures lower than 1 GPa ([Austrheim and Griffin 1985](#)). Incomplete reaction  
136 during the Scandian burial event developed a prograde amphibolite facies (0.8–1.0 GPa

137 ~ 600–650°C ([Glodny et al. 2008](#), [Centrella et al. 2018](#), [Moore et al. 2020](#)) and peak  
138 eclogite facies imprint (2.2 GPa, 690°C; [Bhowany et al. 2018](#)) disseminated inside a  
139 anorthositic and gabbroic complex. The two events (grenvillian and caledonian) were  
140 preserved from later retrogression, restrained to the km-size amphibolite shear zones that  
141 surround the granulite-eclogite massif ([Boundy et al. 1992](#)). For this reason, Holsnøy  
142 partly eclogitized granulites are a precious example of lower continental crust showing the  
143 onset of eclogitization reactions, considered therefore as a field analogue of the of lower  
144 continental crust portions buried at depth under present-day collisional orogens (like  
145 below Tibet for example, [Austrheim and Boundy 1994](#); [Jackson et al. 2004](#); [Labrousse et  
146 al. 2010](#) and references therein).

## 147 **2.2 Eclogitization extent and significance**

148 Mapping of lithologies present in Holsnøy have been described in several petrological  
149 studies since the 1980s ([Austrheim and Griffin 1985](#); [Austrheim 1987](#); [Putnis et al. 2017](#),  
150 [2021](#); [Bhowany et al. 2018](#); [Bras et al. 2021](#); [Jamtveit et al. 2018, 2021](#); [Zertani et al.  
151 2022](#)) and the systematic relationships between eclogitization and strain led to the  
152 definition of: (1) up to km-wide eclogitic shear zones that constitute an anastomosed  
153 network inside the pristine granulite, surrounded by less reacted zones where the  
154 granulite becomes individualized into blocks by a network of thin m-wide eclogite facies  
155 shear zones (breccia zones – [Boundy et al. 1992](#)), (2) zones of static eclogitization  
156 ([Jamtveit et al. 2000, 2016](#); [Zertani et al. 2019, 2022](#); [Putnis et al. 2021](#)) appearing as  
157 diffuse halos sometimes from a central fracture, but also (3) pseudotachylytes and their  
158 damage zones that recrystallize into high-pressure paragenesis (1.5 GPa ~ 680°C  
159 [Bhowany et al. 2018](#); [Petley-Ragan et al. 2018](#)), or into lower pressure paragenesis (1.0  
160 GPa ~ 600°C, [Petley-Ragan et al. 2019](#)).

161 It has been proposed that transformations of granulites during the Caledonian  
162 metamorphism remained partial because of the limited amount of fluids involved in the  
163 reactions ([Austrheim 1987](#); [Jamtveit et al. 1990](#)). Fluid supply is therefore a major  
164 controlling factor for the eclogitization reaction in Holsnøy ([Rubie 1986](#); [Putnis and  
165 Austrheim 2010](#); [Putnis et al. 2017](#); [Centrella 2019](#); [Moore et al. 2020](#); [Zertani et al. 2022](#))

166 and hence the observed associated heterogeneous strain pattern. It has also been  
167 proposed that pressure and stress distribution were actually not homogeneous at the time  
168 of metamorphism and strain ([Jamtveit et al. 2018](#); [Moore et al. 2019](#); [Putnis et al. 2021](#),  
169 [Moulas et al., 2022](#)). The impact of the eclogitization reaction itself has eventually been  
170 proposed to explain the observed intimate relationship between strain and eclogite facies  
171 imprint ([Bras et al. 2021](#)). In this prospect the relative chronology between development  
172 of ductile eclogite facies shear zones, spreading of static eclogite facies halos, and brittle  
173 deformation (pseudotachylytes) as well as the ability of these localized strain zones to  
174 promote fluid percolation are the key evidence for the on-going debate.

### 175 **2.3 Sampling strategy**

176 The relationships between eclogitization front and strain at the shear zone boundaries  
177 have been carefully documented in recent studies ([Bras et al. 2021](#), [Kaatz et al. 2022](#)),  
178 and show that (i) the fluid percolation front is further advanced in the granulite than the  
179 effective reaction front ([Kaatz et al. 2022](#)) and (ii) that the reactions developing at the outer  
180 edge of the strain zone actually involve only part of the bulk rock chemical system and  
181 induce a substantial solid volume change ([Bras et al. 2021](#)). The very first increment of  
182 reactions seem therefore to have a critical effect on the fluid budget and the mechanical  
183 alteration of the granulite. The aim of the present study is to complete the existing dataset  
184 with detailed petrological observations performed at the locus where those very first  
185 reactions increments are expected to be best preserved, i.e. at the tip of a “static” finger  
186 within an overall undeformed granulite block.

187 The rocks studied here were sampled on an outcrop previously described in [Bras et al.](#)  
188 [\(2021\)](#) at the tip of a meter-scale long and decimeter wide eclogite finger ([Figs. 1c-d](#)) that  
189 develops into the granulite along its foliation, underlined in the field by elongated coronas  
190 of garnet, orthopyroxene and clinopyroxene (red and black [Fig. 1d](#); red zones [Fig. 2b](#)).  
191 This finger is rooted in a dextral eclogitic shear zone with an orientation to N110, oblique  
192 to the granulitic foliation, which strikes N020 ([Fig. 1](#), SZ1 [Bras et al., 2021](#)). The orientation  
193 of this shear zone is consistent with the global orientation of the shear at the scale of the  
194 whole massif (i.e., parallel to the major Hundskjefthen shear zone — [Boundy et al. 1992](#);

195 [Zertani et al. 2019](#) and [Fig. 1a](#)). Two thin sections have been prepared through the finger,  
196 from the less reacted granulite to more eclogitized zones ([Figs. 2,3, 4](#)) and are localized  
197 in [Fig. 1d](#) and in the inset of [Fig. 2a](#) (transect T1 at the tip of the finger contains unreacted  
198 granulite whereas transect T2 is more internal, and therefore more eclogitized).

### 199 **3. Methods**

200 Thin sections were analyzed with scanning electron microscopy (SEM) to  
201 backscattered (BSE) images and energy dispersive spectroscopy (EDS) maps. Analyses  
202 were performed at IStEP (Sorbonne Université, Paris) with a ZEISS Supra 55 variable  
203 pressure (VP) SEM-FEG (Field Emission Gun) and at ENS (Paris) with a ZEISS Sigma  
204 SEM-FEG, both equipped with backscattered electron (BSE) and energy dispersive (EDS)  
205 detectors. Operation conditions for EDS maps were set at 15 kV with a spot size of 2.27  
206  $\mu\text{m}$  for large-scale maps, and 10 kV with a spot size of 0.45  $\mu\text{m}$  for small-scale maps, with  
207 a working distance of 15 mm.

208 Quantitative mineral compositions were measured by electron probe micro-  
209 analysis (EPMA) at CAMPARIS facility (Sorbonne Université, Paris) using a CAMECA  
210 SX-100 and SX-FIVE electron microprobes. Working conditions were set to 15 kV  
211 accelerating voltage, 10 nA beam current, 5  $\mu\text{m}$  beam size and 10 s counting time for  
212 major mineral analysis. Albite, orthoclase,  $\text{Fe}_2\text{O}_3$ ,  $\text{MnTiO}_3$ ,  $\text{Cr}_2\text{O}_3$  and diopside were  
213 used as standards. For analcime analysis, they were set to 15 kV accelerating voltage, 4  
214 nA beam current, a counting time of 5 s on the peak for Na, K and Si instead of 10 s for  
215 other elements, and a defocussed beam size of 5  $\mu\text{m}$  in order to avoid Na and K losses  
216 that are expected while analyzing weakly crystallized phases or glasses ([Morgan and](#)  
217 [London 1996, 2005](#)). These two elements were measured first in that respect. The  
218 following reference glasses were used for alkali-loss correction: BCR-2G, BHVO-2G, BIR-  
219 1G.  $\text{H}_2\text{O}$  concentrations in analcime and amorphous pools are calculated by difference of  
220 chemical analyses totals from 100 %.

221 For Electron back-scatter diffraction (EBSD) mapping, thin sections were  
222 additionally polished with colloidal silica. EBSD analyses were carried out at IStEP

223 (Sorbonne Université, Paris) using a ZEISS Supra 55 VP SEM-FEG and at ENS (Paris)  
224 using a ZEISS Sigma SEM-FEG, both equipped with an EBSD detector. Samples were  
225 tilted to 70° during acquisition, with electron beam set to 15 kV, and a beam current of 10  
226 nA at a working distance of 15 mm. At IStEP, data acquisition was performed with a  
227 Quantax Esprit 2.2 software and post-processing done with the same sample software,  
228 whereas at ENS data acquisition was performed with an Oxford Instrument Aztec software  
229 and post-processing done using Oxford Instruments Channel 5.12 software Tango. Post-  
230 processing consisted in applying a wild spike and iterative nearest neighbour corrections.  
231 EBSD data were processed with the Matlab Toolbox MTEX (version 5.3.1) for grain  
232 reconstruction and crystal orientation analysis (Bachmann et al. 2010). Data sets were  
233 cleaned from points with mean angular deviation (MAD) index > 1. Grain boundaries are  
234 defined by misorientations  $\geq 10^\circ$ . Grains  $\leq 3$  pixels were removed. Grain size is calculated  
235 from grain areas ( $A$ ) by the equivalent diameter equation  $d = 2\sqrt{\frac{A}{\pi}}$ . In order to process  
236 EBSD data, plagioclase crystal lattice has been defined from labradorite of the *American*  
237 *Mineralogist's* crystal structure database (Wenk et al. 1980) as follows:  $a = 8.17 \text{ \AA}$ ,  $b =$   
238  $12.87 \text{ \AA}$ ,  $c = 7.10 \text{ \AA}$ ,  $\alpha = 93.46^\circ$ ,  $\beta = 116.05^\circ$ ,  $\gamma = 90.48^\circ$ , and space group is  $P-1$ . Twin  
239 boundaries are defined by misorientations  $> 178^\circ$  between adjacent plagioclase grains,  
240 i.e.,  $\pm 2^\circ$  away from the theoretical  $180^\circ$  around  $b$ -axis rotation associated to albite and  
241 pericline twinning (Figs. 5a, b). Preferential orientation of maximal finite shortening (Z) and  
242 stretching (X) directions for each plagioclase grain were plotted in stereodiagrams after  
243 calculation from plagioclase crystal theory (Lawrence 1970; Borg and Heard 1970;  
244 Egydio-Silva and Mainprice 1999) using pixel orientations in twinned and un-twinned  
245 regions (e.g., Fig. 5c). As albite and pericline twinning systems are orthogonal and contain  
246 each other Burgers vector, focal mechanism-like «beachballs» could be drawn after the  
247 aforementioned stereodiagrams by coloring compression quadrants in white and tension  
248 quadrants in black (e.g., inset Fig. 5c). Note that both twin planes express the same stress  
249 field, but none of them are required to infer from the best strain ellipsoid. Indeed, as their  
250 orientation in the crystal is unique, crystal orientation only is sufficient. Best stress  
251 orientation for activation of plagioclase twinning system can also be inferred from Schmid  
252 factor (SF) calculations. SF is the coefficient that links the component of externally applied

253 stresses normal to the slip plane ( $\sigma_0$ , Fig. 5a) to the resulting shear stresses acting on the  
254 slip plane in the slip direction ( $\tau$ , Fig. 5a), as expressed by the Schmid law:  $\tau = \sigma_0 \times SF$   
255 with  $SF = \cos(\alpha) \times \cos(\beta)$ , with  $\alpha$  the angle between  $\sigma_0$  and the externally applied force,  
256 and  $\beta$  the angle between  $\tau$  and the externally applied force (Fig. 5a). Maximum value of  
257 SF is 0.5 at 45° of slip direction and slip plane pole, as inferred from geometrical  
258 considerations (Fig. 5a), and because twinning system not only has a direction but also a  
259 sense for gliding, minimum SF value is -0.5. For each plagioclase grain analyzed by  
260 EBSD, SF was color-plotted as a spherical function (e.g., Fig. 5c), by calculating the best  
261 stress tensor orientations for each pixel of un-twinned regions in order to activate albite or  
262 pericline twinning systems.

263 Raman analysis were performed at ENS with a Renishaw Invia Raman  
264 microspectrometer equipped with a 514 nm Cobolt laser. The Lithothèque ENS de Lyon  
265 database (<https://lithotheque.ens-lyon.fr/Raman/raman.php>) was used for mineral identification by  
266 peak comparison between reference mineral spectra and spectra that have been acquired  
267 with a 50x objective between 175 cm<sup>-1</sup> and 2062 cm<sup>-1</sup>. Intensities between 2432 cm<sup>-1</sup> and  
268 3886 cm<sup>-1</sup> were additionally collected for water band observation. Resolution was 1.8 cm<sup>-1</sup>,  
269 spectra were integrated over 90 s, and the laser power was 5 mW on the sample.  
270 Acquired spectra were normalized to their maximum intensity.

271 Thermodynamic modelling was used to estimate possible  $P$ - $T$  conditions for  
272 melting, for three different chemical systems and with variable water contents.  
273 Perple\_X\_6.9.1 (Connolly 1990, 2009) was used for this purpose, with the internally  
274 consistent thermodynamic database hp62ver.dat (Holland and Powell 2011). The solution  
275 models are for ternary feldspar (Holland and Powell 2003), epidote (Holland and Powell  
276 2011), garnet (White et al. 2014), clinopyroxene (Green et al. 2007), clinoamphibole  
277 (Green et al. 2016), white mica (White et al. 2014) and melt (Green et al. 2016). We also  
278 performed calculations with the thermodynamic database hp11ver.dat (Holland and  
279 Powell 2011) with the solution model for haplogranitic melt (Holland and Powell 2001;  
280 White et al. 2001) for comparison with the tonalitic melt solution model of Green et al.  
281 (2016). This solution model for the melt is more consistent with our chemical system but  
282 not well constrained at high pressures. Consistent solution models for the other minerals

283 are for ternary feldspar (Fuhrman and Lindsley 1988), epidote (Holland and Powell 2011),  
284 garnet (Holland and Powell 1998), clinopyroxene (Holland and Powell 1996),  
285 clinoamphibole (Diener et al. 2011), and white mica (Coggon and Holland 2002;  
286 Auzanneau et al. 2010).

## 287 4. Results

### 288 4.1. Petrological evolution of a static eclogite facies finger

#### 289 4.1.1. The granulite away from the finger

290 The less reacted granulite analyzed here consists of ferro-magnesian elongated  
291 coronas (~ 30%) that mark the granulitic foliation in an anorthositic matrix (Fig. 2c).  
292 Chemical compositions are given in Table 1 and phase abbreviations are after Kretz  
293 (1983). Coronas are composed of millimeter-sized euhedral grains of garnet  
294 ( $\text{Alm}_{25}\text{Grs}_{19}\text{Py}_{56}$ ), slightly jadeitized clinopyroxene ( $\text{Di}_{64}\text{Hd}_{17}\text{Jd}_{19}$ ) and amphibole. Garnet  
295 is pervasively fractured within a predominant network of ~N040 to N045 fractures (red  
296 arrows in T1, Fig. 2a). Fractures perpendicular to the finger elongation are also  
297 discernable on the more internal transect (red arrows in T2, Fig. S1a). Matrix is composed  
298 of millimeter-sized euhedral grains of plagioclase ( $\text{An}_{41}\text{Ab}_{58}\text{Or}_{01}$ ) with minor isolated  
299 garnets. Other minor phases can be identified within the granulite as Fe-Ti oxides and  
300 apatite (bright minerals Figs. 2a, S1a). This low-transformed area constitutes the first 5  
301 mm from the western part of transect T1, and is almost not present in transect T2.  
302 Eclogitization in this area is limited and is marked by the nucleation of zoisite + K-feldspar  
303 at plagioclase-plagioclase grain boundaries that are 10–20  $\mu\text{m}$  thick (orange arrows in  
304 Figs. 2a, 2c, 3a). Zoisite form sheaves of needles often elongated perpendicular to the  
305 grain boundary, inside diffuse patches of potassium feldspar. The initiation of the reaction  
306 is also characterized by the growth of a thin rim (20–30  $\mu\text{m}$ ) of omphacite at plagioclase-  
307 garnet grain boundaries (Figs. 2c, 3d). Some  $\mu\text{m}$ -thick needles of zoisite and minor kyanite  
308 needles also nucleate inside the plagioclase grains.

#### 309 4.1.2. Evolution toward the finger

310 The amount of zoisite and kyanite found inside plagioclase grains increases toward  
311 the center of the finger. Preferential growth of these minerals is guided by plagioclase  
312 clivages, as underlined by the non-random orientation of zoisite and kyanite long axis (Fig.  
313 2d). Plagioclase in this region is more albitic ( $An_{13}Ab_{86}Or_{01}$ ). Quartz is rarely observed.  
314 The omphacite rim around garnet is thicker than in the less transformed area described  
315 in Section 4.1.1 and takes the form of an outer rim of hundreds of microns thick and an  
316 inner thinner rim, separated by kyanite grains that underline the former plagioclase-garnet  
317 grain boundary (Fig. 2d). These kyanite grains are therefore considered as the remnants  
318 of an early crystallization stage. A clinopyroxene-plagioclase symplectite at grain  
319 boundaries in both rims marks limited retrogression. Omphacite grain-size in these rims  
320 is  $\sim 100 \mu\text{m}$  (Figs. 2d, 3f). Slight zoning in garnet is visible in BSE images (Figs. 2d, 3e)  
321 with a Fe-enriched / Mg-depleted rim ( $Alm_{43}Grs_{17}Py_{40}$ ) free of inclusions and with a  
322 tortuous boundary toward the inner omphacite rim. Although not further elaborated, it is  
323 to be noted that garnet in this area re-equilibrated to eclogite facies conditions as  
324 described by Raimbourg et al. (2007) (equivalent to re-equilibrated garnet II) while the  
325 growth of a Ca-richer eclogitic garnet (garnet III from same authors) is not observed,  
326 except as exsolutions along clinopyroxene crystal planes (as described by Raimbourg  
327 2005). Jadeite component in clinopyroxene increased to  $Di_{34}Hd_{10}Jd_{53}Ts_{03}$ . Chemical  
328 evolution of clinopyroxene as well as fluid flow through the finger have been precisely  
329 described in analogue lithologies (Putnis et al. 2021; Zertani et al. 2022; respectively), and  
330 are therefore not detailed here.

### 331 4.1.3. In the core of the finger

332 Complete breakdown of plagioclase is only reached in the center of the finger, in  
333 zones where the distance between garnet grains is limited ( $<1-2 \text{ mm}$ ) and therefore  
334 allowed diffusion of Na-Si and Ca-Al between garnet and plagioclase (Fig. S1a). In these  
335 zones (Fig. 2e), plagioclase has been totally replaced by an assemblage of omphacite  
336 ( $Di_{35}Hd_{10}Jd_{49}Ts_{06}$ ) and phengite + kyanite + zoisite + apatite + rutile as minor phases.  
337 Kyanite grains underline former grain boundaries between plagioclase and ferro-  
338 magnesian phases (green arrows in Fig. 2a).

## 339 4.2. Strain recorded inside plagioclase grains

340 Intragranular plastic deformation inside plagioclase grains in partially transformed  
341 zone was estimated by calculating the angular difference between average orientation of  
342 each plagioclase grain and individual orientation of pixels belonging to this grain  
343 (Mis2Mean, Fig. 5d). High misorientation angle domains (up to  $6^\circ$ ) are observed within  
344 plagioclase grains and seem limited by zoisite and kyanite inclusions (Fig. 5d), implying  
345 that they arise from strain accumulated during or after inclusions development. Although  
346 albite and pericline twinning in plagioclase can arise both from growth and plastic  
347 deformation. (Borg and Heard 1969; Marshall and McLaren 1977; Smith and Brown 1988),  
348 deformation twins can be identified by morphological criteria. They are usually irregular,  
349 present lenticular forms, and are limited by lattice defects in the grain (as cracks for  
350 example), in opposition to growth twins that have parallel boundaries and strike through  
351 the entire grain (Incel et al., 2022). In the studied plagioclase crystal, we can therefore  
352 infer that twins are related to strain because (i) they are limited by zoisite inclusions (Fig.  
353 5e, 4b), (ii) they are of variable thickness and some are lenticular, and (iii) they correspond  
354 to low misorientation areas (Fig. 5d) and individualize domains of high misorientation, i.e.,  
355 they also accommodate intragranular deformation. Most of the activated twins are albite  
356 twins. Some grains show pericline twins associated with albite twins, but none of the  
357 observed grains show pericline twinning activated only.

358 Plagioclase grains from poorly transformed areas were chosen for SF calculation  
359 (see location on T1 Fig. 6a). They present a various but limited quantity of zoisite and  
360 kyanite grains growing in their interiors. Best orientation for maximum shortening at the  
361 time of twinning formation was deduced from twinned and un-twinned regions orientation  
362 (as in the example of Figs. 5d-f, where deformation twins most probably formed in  
363 response to a shortening of NNE-SSW orientation). This orientation, approximatively  
364 N182,  $42^\circ$ , is visible on the focal mechanism-like «beachballs» stack (Fig. 6b), and  
365 quantitatively specified by the synthetic SF spherical function (Fig. 6c) that was calculated  
366 by stacking and averaging the SF of the regions of Fig. 6a. Orientation map for a  
367 plagioclase grain in a region where the reaction is more advanced (location on Fig. 6a)  
368 has been plotted over band contrast image in Fig. 7. We can see that in this region,

369 plagioclase has been dismantled in small 10  $\mu\text{m}$ -scale plagioclase and zoisite grains (Fig.  
370 7b).

### 371 4.3. Analcime-bearing textures

372 Analcime pools have been identified at former plagioclase-plagioclase grain  
373 boundaries (Fig. 8) in partially transformed zones (white arrows Figs. 2a, S1a), as inferred  
374 from the association with zoisite sheaves of needles typical from former plagioclase-  
375 plagioclase grain boundaries (Fig. 8a). Analcime was identified by Raman analysis (Fig.  
376 9, see also Velde and Besson (1981) for spectra comparison), consistent with microprobe  
377 chemical analysis (Table 2) and EBSD indexing in some limited regions (Fig. S3). Non-  
378 indexing in other regions (Fig. 10) may be due to the high electron beam sensitivity of  
379 such zeolite crystals (Greer and Zhou 2011), or poor crystallinity. Analcime pools are often  
380 porous (red arrow Fig. 8c) and electron beam creates a hole inside them (red arrow Figs.  
381 8b, S4a).

382 Analcime pools which have a diameter of  $\sim 10\text{--}80\ \mu\text{m}$ , present different  
383 morphologies within the sample, but are always associated with kyanite. Indeed, analcime  
384 can form a thin rim ( $< 5\ \mu\text{m}$ ) around kyanite ( $10\text{--}20\ \mu\text{m}$  grain size) that crosscut initial  
385 plagioclase grains forming an alignment of minerals (Figs. 8a,b). When in contact with  
386 plagioclase, analcime pools form cusps with low dihedral angles pointing into plagioclase  
387 (red arrows Figs. 10b,c). Sometimes fine-grained plagioclase ( $< 1\ \mu\text{m}$ ) crystallized  
388 between kyanite grains and analcime pools (Figs. 8a, 10b-e). These late grains are more  
389 calcic ( $\text{An}_{26-29}\text{Ab}_{70-72}\text{Or}_{01-02}$ , Table 2) than plagioclase surrounding the analcime-kyanite-  
390 bearing grain boundary ( $\text{An}_{15}\text{Ab}_{83}\text{Or}_{02}$ , « plagioclase in matrix » in Table 2). Several  
391 kyanite grains associated with analcime contain  $1\text{--}2\ \mu\text{m}$  rounded inclusions of quartz  
392 (Figs. 8a, 10c). In zones where analcime areas really form pools, we can observe the  
393 syntaxial crystallization of K-feldspar (Fig. 8b). Rarely, some euhedral quartz grains also  
394 grow inside the analcime pools (Fig. 8c). Where these particular grain boundaries reach  
395 a ferro-magnesian mineral as garnet or clinopyroxene, analcime pools are not present  
396 and the unique remnant of former grain boundary with plagioclase is kyanite inside the  
397 double omphacite rims (green arrows Fig. 2; red arrow Fig. 8e). The zones where

398 analcime-bearing grain boundaries join omphacite rims are often affected by some  
399 retrogression under the form of a Ca-clinopyroxene+plagioclase symplectite, and  
400 analcime pools there appear surrounded by a thin layer (~4–5  $\mu\text{m}$ ) of the Ca-  
401 clinopyroxene, which indicates that the symplectite develops after formation of these pools  
402 (Fig. 8c). Analcime can also be found associated with zoisite needles (Figs. 8a, 10a). In  
403 some of these regions, zoisite is directly in contact with analcime and presents straight  
404 grain boundaries (Fig. 8a). In other regions (Fig. 10), zoisite is surrounded by fine-grained  
405 plagioclase grains (<1  $\mu\text{m}$ , as described above for kyanite). However, in contrast to  
406 kyanite which presents straight boundaries, plagioclase surrounding zoisite forms cusps  
407 pointing into it with low dihedral angles, so that zoisite boundaries appear tortuous (Fig.  
408 10b). In some places, zoisite ultimately breaks down into anorthite-rich plagioclase. In  
409 these areas, analcime around kyanite progressively transforms into anorthite-rich  
410 plagioclase forming a continuous network from zoisite to kyanite, while analcime pools  
411 seem pseudomorphosed by quartz (Fig. 8f). Analcime also crystallized inside injectite-like  
412 veins that crosscut all the paragenesis (yellow arrows Figs. 2, 8d), and even the  
413 symplectite after omphacite. Chemical composition of analcime in these veins is reported  
414 in Table 2. We did not find any textures indicating that a liquid of analcime composition  
415 could have been injected from the veins into the former plagioclase-plagioclase grain  
416 boundaries, rather the veins seem to crosscut these grain boundaries (Fig. 8d). Reaction  
417 between the veins and the minerals they crosscut is never observed.

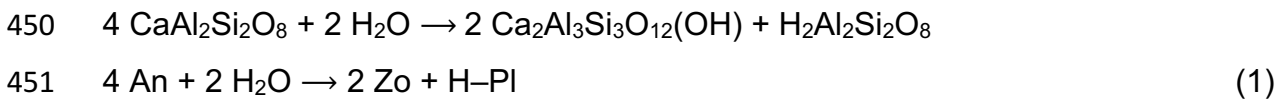
## 418 5. Discussion

419 Our results show that a reaction sequence can be inferred from successive  
420 observations from the pristine granulite (out of the finger) to the core of the « static »  
421 eclogite finger. Such spatial evolution can be interpreted as the time sequence of  
422 successive reactions, following a hydration process from the core to the boundaries of the  
423 eclogite finger (Austrheim 1987; Jamtveit et al. 1990; Jamtveit et al. 2000; Zertani et al.  
424 2022). As no significant deformation occurred in our static eclogite facies finger, the  
425 petrological record we describe here is interpreted as the earliest stage of the  
426 eclogitization process, prior any feedback of strain on reactions. Analcime-bearing  
427 textures and twinning observed within plagioclase could therefore correspond to remnants

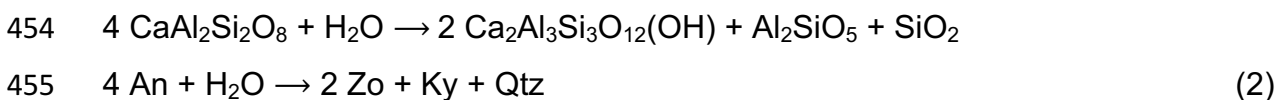
428 of the early eclogitization history. We here discuss this point in the light of previous work.

### 429 **5.1. Reaction sequence preserved through the static eclogitic finger**

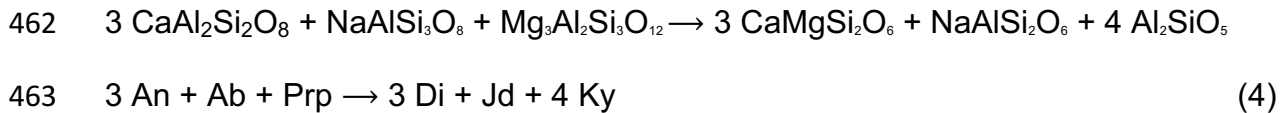
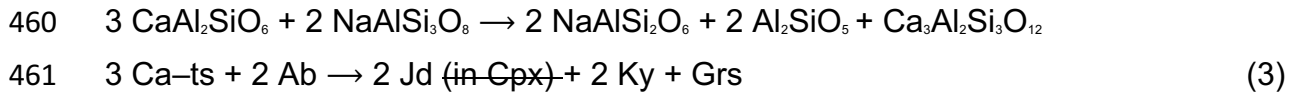
430 Assuming homogeneous  $P$ – $T$  conditions through the whole finger, it is very likely  
431 that the edge-to-core petrological evolution described in Section 4.1 corresponds to a  
432 temporal evolution of the eclogitization. The very beginning stages of reaction would then  
433 have been fossilized at the finger edge, whereas more advanced stages would have been  
434 preserved when approaching the center. This could be due to a two-step fluid diffusion in  
435 the granulite (first fast  $H^+/H_2$ , then slower  $H_2O$ ) as it has been proposed for eclogitic shear  
436 zones in Holsnøy (Kaatz et al., 2022). The observation of potassium being integrated into  
437 K–feldspar in the least transformed areas in opposition to the more transformed domains  
438 where it is integrated into phengite is also in agreement with a gradient in water activity.  
439 In that prospect, we can propose a reaction sequence for the static eclogitization of the  
440 granulite comparable to the ones proposed by Bras et al. (2021) and Kaatz et al. (2022)  
441 for eclogitic shear zones. Although reactions involving a solid solution such as plagioclase  
442 are by definition divariant, the extreme difference in reaction kinetics between the Na and  
443 Ca end-members reactions implies that reactions need to be assessed separately, which  
444 does not imply they are independent. The first reaction grain boundaries involves the Ca  
445 chemical system with the nucleation of zoisite needles intergrown with K-feldspar (Figs.  
446 2c, 3a,b). Then, reaction starts inside plagioclase grains by the nucleation of zoisite and  
447 kyanite needles, which leads to an albitization of the former plagioclase (Fig. 2d). This first  
448 stage of reaction corresponds to the anorthite breakdown reaction that can be written  
449 under the form of:



452 as proposed by Kaatz et al. (2022) for the first step of hydrogen influx into the nominally  
453 anhydrous plagioclase, followed then by the real hydration reaction:



456 (Goldsmith 1982; Wayte et al. 1989), when the solubility of hydrogen in plagioclase is  
457 reached. Na diffusion at plagioclase-ferromagnesian phases grain boundaries then  
458 triggers the formation of omphacite grains, intergrown with kyanite and minor zoisite (Figs.  
459 2d, 3d,e,f), following the reactions:



464 at plagioclase-clinopyroxene and plagioclase-garnet grain boundaries respectively  
465 (Mattey et al. 1994; Schneider et al. 2007). These two reactions can be catalyzed by the  
466 presence of water but do not involve water as a stoichiometric reactant. Grossular is only  
467 found in exsolutions inside clinopyroxene as already described by Raimbourg (2005). The  
468 double omphacite rims separated by a thin layer of kyanite observed around the  
469 ferromagnesian phases (Figs. 2, 3), indicate an early event of kyanite nucleation at  
470 plagioclase-clinopyroxene and plagioclase-garnet grain boundaries that preceded the Na-  
471 diffusion related formation of omphacite. Undulose boundaries of the garnet (Fig. 3d-f)  
472 attest for destabilization of this phase at time of omphacite formation, while its rims evolve  
473 toward the almandine end-member (Table 1) governed by reaction (4). Reactions (2), (3),  
474 and (4) proceed until total breakdown of former plagioclase and Na-Ca equilibration in  
475 omphacite (Fig. 2e), which is rarely the case in our samples.

## 476 5.2. Twinning in plagioclase: a first deformation stage at low differential stress

477 The very first step of plagioclase breakdown during pressure increase and fluid  
478 influx seems to be the nucleation and growth of zoisite. We have shown that it is  
479 associated with strain-related twinning inside plagioclase grains (Fig. 5). Our mechanical  
480 analysis of these twins yields a significant anisotropy with a ~ N-S dipping to the south  
481 maximum compressive stress direction at the time of twinning (Fig. 6b). No clear direction  
482 of minimal compressive stress direction is defined, implying a pure shear regime. This  
483 maximum stress orientation deduced from twinning is close to the pole of the eclogite

484 foliation (i.e., maximal principal shortening) measured for the nearby Hundskjeften zone  
485 ([Zertani et al. 2019](#)), at the termination of which the studied finger has been sampled.  
486 Moreover, such orientation of the stress is also in agreement with the orientation of shear  
487 along eclogite-facies shear zones described by [Raimbourg et al. \(2005\)](#). The well defined  
488 maximum compressive stress direction and poorly defined minimum compressive stress  
489 direction also echoes the axial compression-related finite strain deduced from  
490 Crystallographic Preferred Orientation (CPO) analysis in omphacite from Holsnøy  
491 sheared eclogites ([Bascou et al. 2001](#)). It therefore seems that twinning was controlled by  
492 regional field stress state.

493 On the other hand, most of the twins show clear textural relationship with the zoisite  
494 inclusion network within the grains: most of them are bounded by zoisite-filled cracks, and  
495 their density fades from the cracks toward the inclusion free domains ([Fig. 4](#)), so that  
496 twinning seems to be associated to the zoisite inclusion network development. Twinning  
497 solely associated with grain-scale stresses is expected to yield a homogeneous isotropic  
498 SF density function, as no clear anisotropy is seen in the inclusion pattern. We therefore  
499 have both evidence of regional stress state and local process control on the twinning  
500 pattern, which suggests that the addition of both local and regional stress states has to be  
501 considered.

502 The complete reaction  $\text{anorthite} + \text{H}_2\text{O} = \text{zoisite} + \text{kyanite} + \text{quartz}$ , has a -15% solid  
503 reaction change. The observed crystallization of zoisite or kyanite alone in their host grain  
504 and the necessary export of silica toward grain boundaries implies an even larger local  
505 contraction. In this prospect the development of zoisite inclusions could be seen as an  
506 anticrack system, with significant stress increase at its tips ([Sternlof et al. 2005](#)). This  
507 model would then reconcile the two apparently contradicting observations above, but also  
508 implies that the regional differential stress was lower than the poorly constrained activation  
509 threshold of the albite twinning system. This requires that local stress disturbance due to  
510 the zoisite-in reaction was high enough for the addition of both stress states to yield a  
511 maximum stress above this threshold.

512 An alternative scenario would be to consider twinning as a late feature in regards to zoisite

513 formation. It is indeed expected that inclusion-bearing plagioclase would also have its  
514 twinning domains bounded by the pre-existing inclusions, if they develop later. However,  
515 some recent studies ([Jamtveit et al. 2018](#); [Putnis et al. 2021](#)) argue for the amphibolite  
516 facies event in Holsnøy to be coeval with the eclogite facies state, depending on the  
517 pressure field in the granulites. Therefore, even if linked to the amphibolite facies event,  
518 twinning would have been activated in response to the same stress field than the one  
519 registered by the eclogitic shear zones. However, there is no argument allowing to state  
520 that the considered granulitic bloc would have reached its maximum stress only at the  
521 time of the amphibolitization, while intense deformation has been accommodated by the  
522 surrounding shear zones at the time of eclogitization.

523 In regions where the reaction is more advanced ([Figs. 4,7](#), see location in [Fig. 6a](#)),  
524 plagioclase grain size has been reduced. If twin boundaries were to evolve into new grain  
525 boundaries, the resulting grain size would be even more reduced, to only a few  
526 micrometers ([Fig. 7b, c](#)). This evolution of the twins is consistent with previous studies  
527 that already emphasized the ability for twin boundaries to facilitate subgrain rotation  
528 ([Menegon et al., 2011](#)). Twin planes in plagioclase are also prone to fluid infiltration ([Incel  
529 et al., 2022](#)) or new phases nucleation ([Wayte et al., 1989](#)) as high-angle grain boundaries  
530 are.

### 531 **5.3. Partial melting of the partially eclogitized granulites**

532 In order to assess an eventual partial melting stage in the eclogitization process  
533 developing at the edge of the studied finger, we develop here the textural evidences  
534 supporting the occurrence of a melt at grain boundaries, the  $P-T-X_{H_2O}$  conditions prone  
535 to melting compared to acknowledged  $P-T$  path for the Holsnøy granulites, the expected  
536 composition of melt, how it compares with paragenesis remaining at grain boundaries,  
537 and eventually to what reactions such a partial melting stage can be attributed.

#### 538 **5.3.1. Analcime pools: textural evidence for partial melting?**

539 To our knowledge, it is the first time that analcime pools are described in Holsnøy.  
540 Only rare studies already mentioned zeolite in irregularly shaped pools replacing a former

541 melt (Kiseeva et al. 2017 in mantle xenolites). The recent paper of Liu and Massonne  
542 (2022) constitutes the first study that truly associates analcime pools to crystallization of  
543 a nepheline normative melt, in a garnet clinopyroxenite of the Western Gneiss Region, at  
544 around 600–650°C. Several characteristics of analcime pools described in Section 4.3  
545 constitute arguments for the presence of a former melt, and appear to be very similar to  
546 those described by Liu and Massonne (2022). Indeed, the pools have wedge-like  
547 offshoots, i.e., they form cusps with low dihedral angles toward the host plagioclase (Figs.  
548 S4a, 10b,c), sometimes dendritic morphologies (Fig. 10), and present wavy pool-  
549 plagioclase boundaries (Figs. 8, 10) that are textures typical for crystallization products  
550 from melt (e.g., Tsuchiyama and Takahashi 1983; Holness and Sawyer 2008; Vernon  
551 2011; Ferrero et al. 2012; Liu et al. 2014; Cao et al. 2018). Other textures are similar to  
552 what Liu and Massonne (2022) already described as: (i) the euhedral crystals of quartz  
553 that grew in some of the analcime pools (Fig. 8c), (ii) the thin rim of micro-metric  
554 plagioclase that recrystallized between analcime and kyanite (Fig. 10), (iii) the rim of  
555 diopside that surround the analcime pools when they are in contact with the symplectite  
556 after omphacite (Fig. 8c), and (iv) the euhedral K-feldspar crystals that are growing from  
557 the host plagioclase-pools interface toward the center of analcime pools (Figs. 8b, S4a,b).  
558 This last texture between associated analcime, K-feldspar and albite is common for  
559 magmatic crystallization of hydrous Na-rich melts as described in natural case studies  
560 (e.g., Markl 2001; Analcime I from Pe-Piper et al. 2019) and also stated by experimental  
561 studies that estimated the conditions of analcime crystallization at <650°C, 0.5–1.3 GPa  
562 (Peters et al. 1966; Newton and Kennedy 1968; Boettcher and Wyllie 1969; Kim and  
563 Burley 1971a,b,c, 1980; Liou 1971; Thompson 1973; Roux and Hamilton 1976; Johnson  
564 et al. 1982). Moreover, a subsolidus assemblage analcime + albite + vapor was observed  
565 after crystallization of melt produced at 2 GPa, 750°C in the NASH system (Boettcher and  
566 Wyllie 1969). All these aforementioned characteristics of analcime as found in our  
567 samples allow us to exclude a metasomatic replacement origin of this mineral after albite  
568 or jadeite as it has been observed in some Na-rich environment (Harlow 1994; Harlow et  
569 al. 2011; Tsujimori and Harlow 2012). The close association of kyanite surrounded by  
570 analcime (Figs. 8, 10) and quartz surrounded by a thin film of K-feldspar in some  
571 plagioclase-plagioclase grain boundaries (Fig. S4b) is an additional argument for

572 crystallization from a former melt. Similar quartz–K–feldspar textures have indeed been  
573 characterized as melt filled pores pseudomorphs in migmatites by several studies  
574 (Holness and Sawyer 2008; Vernon 2011). We suggest that the rim of kyanite that  
575 separates the double omphacite rim around ferro-magnesian phases could be the  
576 remnant of analcime-kyanite bearing grain boundaries as described between plagioclase-  
577 plagioclase grains.

### 578 **5.3.2. $P$ – $T$ – $X_{H_2O}$ conditions prone to partial melting**

579 To elaborate on the possible conditions for partial melting of our transforming  
580 granulite, we calculated  $P$ – $T$  and  $P$ – $X_{H_2O}$  pseudosections with the tonalitic melt solution  
581 model from Green et al. (2016) which is the only one constrained at pressures up to 1.3  
582 GPa and often used for calculations at these pressures (e.g., Putnis et al. 2021; Liu and  
583 Massonne 2022). Results of the calculations are presented in Fig. 11 and Fig. S6 (see  
584 Method section for details). Calculations with the haplogranitic melt solution model from  
585 Holland and Powell (2001) and White et al. (2001) have also been performed (Fig. S5,  
586 S6) but considered as poorly constrained for our samples in the eclogite  $P$ – $T$  range. We  
587 performed the calculation for three different effective compositions (Table 3) in order to  
588 examine the possibility for partial melting of our samples at different stages of equilibration  
589 during the ongoing eclogitization. For local equilibrium at different stages of plagioclase  
590 breakdown in matrix domains, we use (1) the pristine plagioclase composition of our  
591 granulite facies area (Granulite Table 1, and  $Pl_0$  Table 3) and (2) the more albite-rich  
592 composition of plagioclase in partially eclogitized area (Table 1 and  $Pl_1$  Table 3) in the  
593 CKNASH system. Depending on the effective local chemical system considered,  
594 thermodynamic modelling indicates that partial melting is possible near the peak  $P$ – $T$ –  
595  $X_{H_2O}$  conditions experienced by our samples provided that: (i) the local water content is  
596  $\geq 0.4$  wt% for albitized plagioclase chemical system, or (ii) pressure drops down to 1.6  
597 GPa or temperature rises to 730°C for a fully hydrated (1 wt% H<sub>2</sub>O) initial plagioclase  
598 chemical system. As already asserted by Liu and Massonne (2022) according to  
599 experimental studies (Peters et al. 1966; Roux and Hamilton 1976) analcime can coexist  
600 with melt at temperatures  $\leq 650^\circ\text{C}$  at eclogite facies pressures and could therefore have  
601 crystallized just below 650°C at the time of symplectite crystallization. The observed

602 injectite-like veins filled by analcime as described in Section 4.3, crosscut all the  
603 paragenesis, including the analcime-kyanite grain boundaries as well as the symplectite  
604 after omphacite (yellow arrows [Figs. 2, 8d](#)). Neither the temporal nor the genetic  
605 relationships between these analcime veins and analcime-kyanite grain boundaries can  
606 be unequivocally determined, but it is obvious that injection of the veins corresponds to a  
607 late event, at least post-dating the retrogression into symplectite, while the analcime-  
608 kyanite grain boundaries constitute an early stage in the rock evolution. Veins could on  
609 one hand correspond to a late injection of a melt of analcime composition, formed at higher  
610 pressures and maintained liquid during the retrograde path. Volume increase caused by  
611 the melt decompression could have fractured the host rock. It is on the other hand unlikely  
612 that injection veins came from a low pressure pseudotachylyte further away in the outcrop  
613 that we did not see while sampling since no analcime-bearing pseudotachylyte remnants  
614 has ever been described in Holsnøy, and melt produced in pseudotachylytes have initial  
615 compositions close to their host-rock ([Zhong et al. 2021](#)).

### 616 **5.3.3. Expected composition of the melt**

617 Melt compositions from thermodynamic calculations are roughly constant on the  
618 whole range of  $P$ - $T$ - $X_{H_2O}$  conditions, and regardless of the solution model chosen for melt.  
619 All compositions cluster close to 58 SiO<sub>2</sub>; 14 Al<sub>2</sub>O<sub>3</sub>; 1 CaO; 6 Na<sub>2</sub>O; 1 K<sub>2</sub>O; 20 H<sub>2</sub>O in wt  
620 % so they are quartz and corundum normative (9 and 1 wt% respectively) instead of being-  
621 nepheline normative as expected if considering analcime pools as a crystallized former  
622 melt. This inconsistency was also highlighted by [Liu and Massonne \(2022\)](#) but as they  
623 stated, very few studies already described this type of partial melting phenomena,  
624 particularly in K-poor high-pressure rocks like those described here. Moreover, melt  
625 models are not well constrained at such high pressures so compositions extracted from  
626 thermodynamic modelling should be cautiously handled. It is also highly possible that  
627 analcime only represents the final crystallization of the last liquid phase and that initial  
628 melt composition was different. In addition, compilation from both natural and  
629 experimental data ([Labrousse et al. 2011](#)) emphasized that high-pressure melts evolve  
630 toward more Na-rich compositions (i.e., trondhjemitic) with increasing pressure. Hence, it  
631 is probable that a melt formed at 2 GPa would be Na-rich, and possibly enough to lead to

632 the eventual crystallization of such a Na-rich phase as analcime.

#### 633 **5.3.4. Partial melting reactions**

634 Textural observations as described in Section 5.3.1 emphasized the  
635 association of kyanite, zoisite, plagioclase and analcime in the partial melting textures. In  
636 regions where analcime pools are present, zoisite grain boundaries are tortuous, and they  
637 are only found at initial plagioclase-analcime contact zones but totally absent from the  
638 center of these regions (Fig. 10). Thus, it appears highly possible that zoisite was  
639 consumed by the partial melting reaction. While textures evidence that analcime and  
640 plagioclase recrystallized grains around kyanite result from crystallization after a melt, it  
641 is more difficult to decipher the implication of kyanite in the partial melting process. A  
642 possible melting reaction would be  $Zo + Ab + Qtz \rightarrow Melt + Ky$ , which constitutes a  
643 plagioclase-involving version of the reaction  $Zo + NaAl-Cpx + Qtz \rightarrow Melt + Ky + CaMg-$   
644  $Cpx$  proposed by Skjerlie and Patiño Douce (2002) for zoisite dehydration melting at high  
645 pressures. In this reaction quartz is consumed. This could constitute an explanation to the  
646 general lack of quartz in our sample. Moreover, this is in agreement with experimental  
647 studies in the NASH system (Boettcher and Wyllie 1969) which proposed that metastable  
648 plagioclase could be involved in melting reactions in the presence of free fluid. The  
649 resulting melt can in a second time crystallize into  $Anl + Qtz + Pl + Fluid$  which in turn  
650 could explain the association of analcime with quartz and kyanite, and also the  
651 crystallization of small plagioclase grains around kyanite.

652 Zoisite dehydration melting at water absent conditions is reached at temperatures  
653 much higher than the one reached by our samples (Skjerlie and Patiño Douce 2002; Cao  
654 et al. 2018). However, at water present conditions, melting of zoisite has been described  
655 at reasonable temperatures at 2 GPa (~800°C for zoisite + kyanite + quartz + vapor =  
656 melt, Schmidt and Poli 2004), depending on the chemical system involved. Schmidt and  
657 Poli (2004) also showed that in the presence of a K-bearing phase, zoisite melting  
658 reactions would take place at even lower temperatures, e.g., the reaction zoisite + white  
659 mica + quartz + vapor = kyanite + melt at 725°C – 2 GPa.

660 As a conclusion, we propose that textural evidence point toward a limited partial

661 melting stage, due to zoisite and metastable Na-rich plagioclase melting in the local  
662 presence of a free fluid, at conditions close the acknowledged peak in the eclogite facies  
663 provided a transient hydration level higher than 0.4 wt%, a limited temperature increase  
664 or a limited pressure decrease.

#### 665 **5.4. Implications for the early mechanical alteration of the reacting granulite**

666 Our structural analysis of twins in plagioclase with no shape preferred orientation  
667 (i.e., not significantly strained) implies that differential stress for twinning was lower than  
668 the creep strength of plagioclase. Twinning activation threshold in plagioclase is poorly  
669 documented but experiments indicate a plastic yield close to 100 MPa at 800°C, 1 GPa  
670 (Borg and Heard 1969). A renewed estimate would ultimately constitute a missing  
671 paleopiezometer for deformation of rocks at high confining pressure strain in the lower  
672 crust.

673 Partial melting at high pressure in the presence of H<sub>2</sub>O-rich fluids has already been  
674 described in the Western Gneiss Region (Labrousse et al. 2002; Ganzhorn et al. 2014;  
675 Liu and Massonne 2022). Major implications on the rheology and strength of the  
676 continental crust have been highlighted, like the important weakening the presence of  
677 such a melt could induce (Rosenberg and Handy 2005; Vanderhaeghe 2009; Brown 2010;  
678 Wang et al. 2014). This weakening can be responsible for the decoupling between the  
679 lower crust and the rest of the subducting slab, and the following exhumation. In the island  
680 of Holsnøy, felsic pegmatite veins intruding the high-pressure eclogites have already been  
681 described and associated with the crystallization after partial melting of the eclogites (of  
682 felsic to intermediate composition) at peak *P–T* conditions and in the presence of a H<sub>2</sub>O-  
683 rich fluid (Andersen et al. 1991). A recent study of Jamtveit et al. (2021) also described  
684 pegmatites and dykes intrusions in the Lindås nappe and proposed the anorthositic  
685 granulites of Holsnøy as possible source for the melts that crystallized in these intrusions.  
686 1.3–1.5 GPa, 710–750°C and 2–4 wt% H<sub>2</sub>O conditions were proposed for partial melting  
687 with temperature increase driven by shear heating at the base of the Lindås nappe.  
688 Melting is possible in plagioclase after zoisite formation at the same temperature as  
689 proposed by Jamtveit et al. (2021), even at pressures and water contents that have been

690 estimated for the eclogite peak conditions. A slight increase in temperature due reaction  
691 enthalpy release (Zertani et al. 2022) or a transient pressure drop cannot be excluded.  
692 Indeed, both stress and pressure field at the tip of the propagating eclogite finger are  
693 expected to be transiently disturbed by (i) the volume change associated with plagioclase  
694 breakdown, as at the tip of an elongated inclusion (Sternlof et al. 2005; Yamato et al.  
695 2022), or (ii) strength drop due to eclogitization (Mancktelow 2008; Moulas et al. 2014),  
696 the combination of the two being also possible. The part of the rock located at the tip of  
697 the finger (Fig. 12) may transiently pass from an over-pressurized domain to an under-  
698 pressurized domain while the finger propagates. The estimated 0.4 GPa decompression  
699 necessary for partial melting at constant temperature (Fig. 11) can therefore be reached  
700 at a background pressure of 2.0 GPa. It is to be noted that while the over-pressurized  
701 domain remains limited to the very tip of the propagating finger, under-pressure is  
702 expected to affect a much wider area along the finger walls. Once initiated, partial melting,  
703 if occurring at fluid present conditions (as proposed in Section 5.3.4), can also enhance  
704 the negative volume change already initiated by the eclogitization reaction (Clemens and  
705 Droop 1998) and further amplify the stress/pressure field disturbance at the tip of the  
706 finger.

707 Even though observations and thermodynamic modelling in the present study point  
708 toward limited partial melting extent, well below any Rheologically Critical Melt Percentage  
709 (RCMP ~ 7%, Rosenberg and Handy 2001), the transient presence of a melt phase in the  
710 plagioclase matrix at grain boundaries may also activate deformation mechanisms, such  
711 as melt-assisted switch from dislocation creep to diffusion creep (Dimanov et al. 2000;  
712 Nasipuri and Bhattacharya 2007). If fluid infiltration precedes the development of eclogite  
713 facies shear zones, as currently acknowledged (Austrheim 1987, 2013; Jamtveit et al.  
714 1990), such processes could also be part of the transient weakening mechanisms needed  
715 to explain widening of eclogite facies shear zones during their development (Bras et al.  
716 2021, Kaatz et al. 2021).

## 717 **6. Conclusions**

718 Eclogitization of rocks is a continuous process that involves multiple breakdown

719 reactions of different kinetics and mechanical implications, during increasing pressure. In  
720 anorthosites where plagioclase constitutes the principal reactive system, these reactions  
721 are often delayed because of the sluggishness of NaSi-CaAl interdiffusion in water-limited  
722 environments. Transient parageneses and textures can therefore persist metastably  
723 through the whole  $P$ - $T$  history of the rock, and control its mechanical behavior. Early  
724 stages of these plagioclase breakdown reactions have been preserved within the  
725 undeformed partially eclogitized granulites studied. Transformation proceeds differently  
726 inside the protolith plagioclase grains and at their boundaries. In both cases, zoisite  
727 crystallization has a first order impact. Indeed, zoisite nucleation and growth inside the  
728 grains distort the plagioclase crystal lattice acting as defects for the activation of twinning  
729 in response to far field stresses. At former grain boundaries, kyanite-analcime association  
730 attests of a partial melting event that could have affected the rocks near the peak  $P$ - $T$   
731 conditions in response to water infiltration, local  $P$ - $T$  changes, or transient changes in the  
732 effective chemical system due to zoisite crystallization. Grain size reduction took place in  
733 the whole transforming rock via the crystallization of small grains from a melt, as well as  
734 after an event of twinning under stress that triggered the creation of new grain boundaries.  
735 This may contribute to mechanical alteration of the reacting granulite over probably short  
736 timescales, not mentioning effective viscosity drop induced by even small volumes of melt  
737 production at grain boundaries. Rheological contrasts generated between partially  
738 transformed and preserved granulite then predispose the rock to potential further  
739 localization of the deformation.

## 740 **References cited**

- 741 Andersen, T., Austrheim, H., & Burke, E. A. J. (1991). Mineral-fluid-melt interactions in  
742 high-pressure shear zones in the Bergen Arcs nappe complex, Caledonides of W.  
743 Norway: Implications for the fluid regime in Caledonian eclogite-facies  
744 metamorphism. *Lithos*, 27(3), 187-204. [https://doi.org/10.1016/0024-4937\(91\)90012-A](https://doi.org/10.1016/0024-4937(91)90012-A)
- 745 Andersen, T. B., Corfu, F., Labrousse, L., & Osmundsen, P. T. (2012). Evidence for  
746 hyperextension along the pre-Caledonian margin of Baltica. *Journal of the Geological*  
747 *Society*, 169(5), 601-612. <https://doi.org/10.1144/0016-76492012-011>

748 Austrheim, H. (1987). Eclogitization of lower crustal granulites by fluid migration through  
749 shear zones. *Earth and Planetary Science Letters*, 81(2-3), 221-232.  
750 [https://doi.org/10.1016/0012-821X\(87\)90158-0](https://doi.org/10.1016/0012-821X(87)90158-0)

751 Austrheim, H. (1991). Eclogite formation and dynamics of crustal roots under continental  
752 collision zones. *Terra Nova*, 3(5), 492-499. [https://doi.org/10.1111/j.1365-  
753 3121.1991.tb00184.x](https://doi.org/10.1111/j.1365-3121.1991.tb00184.x)

754 Austrheim, H. (2013). Fluid and deformation induced metamorphic processes around  
755 Moho beneath continent collision zones: Examples from the exposed root zone of the  
756 Caledonian mountain belt, W-Norway. *Tectonophysics*, 609, 620-635.  
757 <https://doi.org/10.1016/j.tecto.2013.08.030>

758 Austrheim, H., & Griffin, W. L. (1985). Shear deformation and eclogite formation within  
759 granulite-facies anorthosites of the Bergen Arcs, western Norway. *Chemical  
760 Geology*, 50(1-3), 267-281. [https://doi.org/10.1016/0009-2541\(85\)90124-X](https://doi.org/10.1016/0009-2541(85)90124-X)

761 Austrheim, H., & Boundy, T. M. (1994). Pseudotachylytes generated during seismic  
762 faulting and eclogitization of the deep crust. *Science*, 265(5168), 82-83.  
763 [10.1126/science.265.5168.82](https://doi.org/10.1126/science.265.5168.82)

764 Auzanneau, E., Schmidt, M. W., Vielzeuf, D., & D Connolly, J. A. (2010). Titanium in  
765 phengite: a geobarometer for high temperature eclogites. *Contributions to Mineralogy and  
766 Petrology*, 159(1), 1-24. <https://doi.org/10.1007/s00410-009-0412-7>

767 Bachmann, F., Hielscher, R., & Schaeben, H. (2010). Texture analysis with MTEX—  
768 free and open source software toolbox. In *Solid State Phenomena* (Vol. 160, pp.  
769 63-68). Trans Tech Publications Ltd.  
770 <https://doi.org/10.4028/www.scientific.net/SSP.160.63>

771 Bascou, J., Barruol, G., Vauchez, A., Mainprice, D., & Eglydio-Silva, M. (2001). EBSD-  
772 measured lattice-preferred orientations and seismic properties of  
773 eclogites. *Tectonophysics*, 342(1-2), 61-80. <https://doi.org/10.1016/S0040->

774 [1951\(01\)00156-1](#)

775 Bhowany, K., Hand, M., Clark, C., Kelsey, D. E., Reddy, S. M., Pearce, M. A., ... &  
776 Morrissey, L. J. (2018). Phase equilibria modelling constraints on P–T conditions during  
777 fluid catalysed conversion of granulite to eclogite in the Bergen Arcs, Norway. *Journal of*  
778 *Metamorphic Geology*, 36(3), 315-342. <https://doi.org/10.1111/jmg.12294>

779 Bingen, B., Davis, W. J., & Austrheim, H. (2001). Zircon U-Pb geochronology in the  
780 Bergen arc eclogites and their Proterozoic protoliths, and implications for the pre-  
781 Scandian evolution of the Caledonides in western Norway. *Geological Society of America*  
782 *Bulletin*, 113(5), 640-649. [https://doi.org/10.1130/0016-](https://doi.org/10.1130/0016-7606(2001)113<0640:ZUPGIT>2.0.CO;2)  
783 [7606\(2001\)113<0640:ZUPGIT>2.0.CO;2](https://doi.org/10.1130/0016-7606(2001)113<0640:ZUPGIT>2.0.CO;2)

784 Bingen, B., Austrheim, H., Whitehouse, M. J., & Davis, W. J. (2004). Trace element  
785 signature and U–Pb geochronology of eclogite-facies zircon, Bergen Arcs, Caledonides  
786 of W Norway. *Contributions to Mineralogy and Petrology*, 147(6), 671-683.  
787 <https://doi.org/10.1007/s00410-004-0585-z>

788 Boettcher, A. L., & Wyllie, P. J. (1969). Phase relationships in the system NaAlSiO<sub>4</sub>-SiO<sub>2</sub>-H<sub>2</sub>O to 35 kilobars pressure. *American Journal of Science*, 267(8), 875-909.  
789 <https://doi.org/10.2475/ajs.267.8.875>

791 Borg, I. Y., & Heard, H. C. (1969). Mechanical twinning and slip in experimentally  
792 deformed plagioclases. *Contributions to Mineralogy and Petrology*, 23(2), 128-135.  
793 <https://doi.org/10.1007/BF00375174>

794 Borg, I. Y., & Heard, H. C. (1970). Experimental deformation of plagioclases. *Experimental*  
795 *and Natural Rock Deformation*, (pp. 375-403). [https://doi.org/10.1007/978-3-642-95187-](https://doi.org/10.1007/978-3-642-95187-9_15)  
796 [9\\_15](https://doi.org/10.1007/978-3-642-95187-9_15)

797 Boundy, T. M., Fountain, D. M., & Austrheim, H. (1992). Structural development and  
798 petrofabrics of eclogite facies shear zones, Bergen Arcs, western Norway: implications for  
799 deep crustal deformational processes. *Journal of Metamorphic Geology*, 10(2), 127-146.

800 <https://doi.org/10.1111/j.1525-1314.1992.tb00075.x>

801 Bras, E., Baïssset, M., Yamato, P., & Labrousse, L. (2021). Transient weakening during  
802 the granulite to eclogite transformation within hydrous shear zones (Holsnøy,  
803 Norway). *Tectonophysics*, 819, 229026. <https://doi.org/10.1016/j.tecto.2021.229026>

804 Brodie, K. H., & Rutter, E. H. (1985). On the relationship between deformation and  
805 metamorphism, with special reference to the behavior of basic rocks. In *Metamorphic*  
806 *reactions* (pp. 138-179). Springer, New York, NY. [10.1007/978-1-4612-5066-1\\_6](https://doi.org/10.1007/978-1-4612-5066-1_6)

807 Brown, M. (2010). Melting of the continental crust during orogenesis: the thermal,  
808 rheological, and compositional consequences of melt transport from lower to upper  
809 continental crust. *Canadian Journal of Earth Sciences*, 47(5), 655-694.  
810 <https://doi.org/10.1139/E09-057>

811 Cao, W., Gilotti, J. A., Massonne, H. J., Ferrando, S., & Foster Jr, C. T. (2019). Partial  
812 melting due to breakdown of an epidote-group mineral during exhumation of ultrahigh-  
813 pressure eclogite: An example from the North-East Greenland Caledonides. *Journal of*  
814 *Metamorphic Geology*, 37(1), 15-39. <https://doi.org/10.1111/jmg.12447>

815 Centrella, S., Putnis, A., Lanari, P., & Austrheim, H. (2018). Textural and chemical  
816 evolution of pyroxene during hydration and deformation: a consequence of retrograde  
817 metamorphism. *Lithos*, 296, 245-264. <https://doi.org/10.1016/j.lithos.2017.11.002>

818 Centrella, S. (2019). The granulite-to eclogite-and amphibolite-facies transition: a volume  
819 and mass transfer study in the Lindås Nappe, Bergen Arcs, west Norway. *Geological*  
820 *Society, London, Special Publications*, 478(1), 241-264. <https://doi.org/10.1144/SP478.9>

821 Clemens, J. D., & Droop, G. T. R. (1998). Fluids, P–T paths and the fates of anatectic  
822 melts in the Earth's crust. *Lithos*, 44(1-2), 21-36. [https://doi.org/10.1016/S0024-](https://doi.org/10.1016/S0024-4937(98)00020-6)  
823 [4937\(98\)00020-6](https://doi.org/10.1016/S0024-4937(98)00020-6)

824 Coggon, R., & Holland, T. J. B. (2002). Mixing properties of phengitic micas and revised  
825 garnet-phengite thermobarometers. *Journal of Metamorphic Geology*, 20(7), 683-696.

- 826 <https://doi.org/10.1046/j.1525-1314.2002.00395.x>
- 827 Connolly, J. A. D. (1990). Multivariable phase diagrams; an algorithm based on  
828 generalized thermodynamics. *American Journal of Science*, 290(6), 666-718.  
829 <https://doi.org/10.2475/ajs.290.6.666>
- 830 Connolly, J. A. D. (2009). The geodynamic equation of state: what and  
831 how. *Geochemistry, Geophysics, Geosystems*, 10(10).  
832 <https://doi.org/10.1029/2009GC002540>
- 833 Diener, J. F. A., & Powell, R. (2012). Revised activity–composition models for  
834 clinopyroxene and amphibole. *Journal of Metamorphic Geology*, 30(2), 131-142.  
835 <https://doi.org/10.1111/j.1525-1314.2011.00959.x>
- 836 Dimanov, A. W. R. D., Wirth, R., & Dresen, G. (2000). The effect of melt distribution on  
837 the rheology of plagioclase rocks. *Tectonophysics*, 328(3-4), 307-327.  
838 [https://doi.org/10.1016/S0040-1951\(00\)00214-6](https://doi.org/10.1016/S0040-1951(00)00214-6)
- 839 Egydio-Silva, M., & Mainprice, D. (1999). Determination of stress directions from  
840 plagioclase fabrics in high grade deformed rocks (Além Paraíba shear zone, Ribeira fold  
841 belt, southeastern Brazil). *Journal of Structural Geology*, 21(12), 1751-1771.  
842 [https://doi.org/10.1016/S0191-8141\(99\)00121-2](https://doi.org/10.1016/S0191-8141(99)00121-2)
- 843 Ferrero, S., Bartoli, O., Cesare, B., Salvioli-Mariani, E., Acosta-Vigil, A., Cavallo, A., ... &  
844 Battiston, S. (2012). Microstructures of melt inclusions in anatectic metasedimentary  
845 rocks. *Journal of Metamorphic Geology*, 30(3), 303-322. <https://doi.org/10.1111/j.1525-1314.2011.00968.x>
- 847 Früh-Green, G. L. (1994). Interdependence of deformation, fluid infiltration and reaction  
848 progress recorded in eclogitic metagranitoids (Sesia Zone, Western Alps). *Journal of*  
849 *Metamorphic Geology*, 12(3), 327-343. <https://doi.org/10.1111/j.1525-1314.1994.tb00026.x>
- 851 Fuhrman, M. L., & Lindsley, D. H. (1988). Ternary-feldspar modeling and

852 thermometry. *American mineralogist*, 73(3-4), 201-215.

853 Ganzhorn, A. C., Labrousse, L., Prouteau, G., Leroy, C., Vrijmoed, J. C., Andersen, T. B.,  
854 & Arbaret, L. (2014). Structural, petrological and chemical analysis of syn-kinematic  
855 migmatites: Insights from the Western Gneiss Region, Norway. *Journal of Metamorphic*  
856 *Geology*, 32(6), 647-673. <https://doi.org/10.1111/jmg.12084>

857 Glodny, J., Kühn, A., & Austrheim, H. (2008). Geochronology of fluid-induced eclogite and  
858 amphibolite facies metamorphic reactions in a subduction–collision system, Bergen Arcs,  
859 Norway. *Contributions to Mineralogy and Petrology*, 156(1), 27-48.  
860 <https://doi.org/10.1007/s00410-007-0272-y>

861 Goldsmith, J. R. (1982). Plagioclase stability at elevated temperatures and water  
862 pressures. *American Mineralogist*, 67(7-8), 653-675.

863 Green, E., Holland, T., & Powell, R. (2007). An order-disorder model for omphacitic  
864 pyroxenes in the system jadeite-diopside-hedenbergite-acmite, with applications to  
865 eclogitic rocks. *American Mineralogist*, 92(7), 1181-1189.  
866 <https://doi.org/10.2138/am.2007.2401>

867 Greer, H. F., & Zhou, W. (2011). Electron diffraction and HRTEM imaging of beam-  
868 sensitive materials. *Crystallography reviews*, 17(3), 163-185.  
869 <https://doi.org/10.1080/0889311X.2010.535525>

870 Green, E. C. R., White, R. W., Diener, J. F. A., Powell, R., Holland, T. J. B., & Palin, R. M.  
871 (2016). Activity–composition relations for the calculation of partial melting equilibria in  
872 metabasic rocks. *Journal of Metamorphic Geology*, 34(9), 845-  
873 869. <https://doi.org/10.1111/jmg.12211>

874 Hacker, B. R., Peacock, S. M., Abers, G. A., & Holloway, S. D. (2003). Subduction factory  
875 2. Are intermediate-depth earthquakes in subducting slabs linked to metamorphic  
876 dehydration reactions?. *Journal of Geophysical Research: Solid*  
877 *Earth*, 108(B1). <https://doi.org/10.1029/2001JB001129>

878 Harlow, G. E. (1994). Jadeitites, albitites and related rocks from the Motagua Fault Zone,  
879 Guatemala. *Journal of Metamorphic Geology*, 12(1), 49-68.  
880 <https://doi.org/10.1111/j.1525-1314.1994.tb00003.x>

881 Harlow, G. E., Sisson, V. B., & Sorensen, S. S. (2011). Jadeitite from Guatemala: new  
882 observations and distinctions among multiple occurrences. *Geologica Acta*, 363-387.

883 Hetényi, G., Chanard, K., Baumgartner, L. P., & Herman, F. (2021). Metamorphic  
884 transformation rate over large spatial and temporal scales constrained by geophysical  
885 data and coupled modelling. *Journal of Metamorphic Geology*, 39(9), 1131-  
886 1143. <https://doi.org/10.1111/jmg.12604>

887 Holland, T. J. (1980). The reaction albite = jadeite + quartz determined experimentally in  
888 the range 600–1200 C. *American Mineralogist*, 65(1-2), 129-134.

889 Holland, T., & Powell, R. (1996). Thermodynamics of order-disorder in minerals: II.  
890 Symmetric formalism applied to solid solutions. *American Mineralogist*, 81(11-12), 1425-  
891 1437. <https://doi.org/10.2138/am-1996-11-1215>

892 Holland, T. J. B., & Powell, R. T. J. B. (1998). An internally consistent thermodynamic data  
893 set for phases of petrological interest. *Journal of metamorphic Geology*, 16(3), 309-343.  
894 <https://doi.org/10.1111/j.1525-1314.1998.00140.x>

895 Holland, T. I. M., & Powell, R. (2001). Calculation of phase relations involving haplogranitic  
896 melts using an internally consistent thermodynamic dataset. *Journal of Petrology*, 42(4),  
897 673-683. <https://doi.org/10.1093/petrology/42.4.673>

898 Holland, T., & Powell, R. (2003). Activity–composition relations for phases in petrological  
899 calculations: an asymmetric multicomponent formulation. *Contributions to Mineralogy and*  
900 *Petrology*, 145(4), 492-501. <https://doi.org/10.1007/s00410-003-0464-z>

901 Holland, T. J. B., & Powell, R. (2011). An improved and extended internally consistent  
902 thermodynamic dataset for phases of petrological interest, involving a new equation of  
903 state for solids. *Journal of metamorphic Geology*, 29(3), 333-383.

904 <https://doi.org/10.1111/j.1525-1314.2010.00923.x>

905 Holness, M. B., & Sawyer, E. W. (2008). On the pseudomorphing of melt-filled pores  
906 during the crystallization of migmatites. *Journal of Petrology*, 49(7), 1343-1363.  
907 <https://doi.org/10.1093/petrology/egn028>

908 Incel, S., Labrousse, L., Hilairet, N., John, T., Gasc, J., Shi, F., ... & Schubnel, A. (2019).  
909 Reaction-induced embrittlement of the lower continental crust. *Geology*, 47(3), 235-238.  
910 <https://doi.org/10.1130/G45527.1>

911 Incel, S., Baïssset, M., Labrousse, L., & Schubnel, A. (2022) Partial melting and reaction  
912 along deformation features in plagioclase. *Journal of Metamorphic Geology*.  
913 <https://doi.org/10.1111/jmg.12702>

914 Jackson, J. A., Austrheim, H., McKenzie, D., & Priestley, K. (2004). Metastability,  
915 mechanical strength, and the support of mountain belts. *Geology*, 32(7), 625-628.  
916 <https://doi.org/10.1130/G20397.1>

917 Jakob, J., Andersen, T. B., Mohn, G., Kjøll, H. J., & Beyssac, O. (2022). Revised tectono-  
918 stratigraphic scheme for the Scandinavian Caledonides and its implications for our  
919 understanding of the Scandian orogeny. *Geol. Soc. Am. Spec. Paper*. In *New*  
920 *Developments in the Appalachian-Caledonian-Variscan Orogen*.  
921 [https://doi.org/10.1130/2022.2554\(14\)](https://doi.org/10.1130/2022.2554(14))

922 Jamtveit, B., Bucher-Nurminen, K., & Austrheim, H. (1990). Fluid controlled eclogitization  
923 of granulites in deep crustal shear zones, Bergen arcs, Western Norway. *Contributions to*  
924 *Mineralogy and Petrology*, 104(2), 184-193. <https://doi.org/10.1007/BF00306442>

925 Jamtveit, B., Austrheim, H., & Malthe-Sørensen, A. (2000). Accelerated hydration of the  
926 Earth's deep crust induced by stress perturbations. *Nature*, 408(6808), 75-78.  
927 <https://doi.org/10.1038/35040537>

928 Jamtveit, B., Austrheim, H., & Putnis, A. (2016). Disequilibrium metamorphism of stressed  
929 lithosphere. *Earth-Science Reviews*, 154, 1-13.

930 <https://doi.org/10.1016/j.earscirev.2015.12.002>

931 Jamtveit, B., Moulas, E., Andersen, T. B., Austrheim, H., Corfu, F., Petley-Ragan, A., &  
932 Schmalholz, S. M. (2018). High pressure metamorphism caused by fluid induced  
933 weakening of deep continental crust. *Scientific Reports*, 8(1), 1-8.  
934 <https://doi.org/10.1038/s41598-018-35200-1>

935 Jamtveit, B., Petley-Ragan, A., Incel, S., Dunkel, K. G., Aupart, C., Austrheim, H., ... &  
936 Renard, F. (2019). The effects of earthquakes and fluids on the metamorphism of the  
937 lower continental crust. *Journal of Geophysical Research: Solid Earth*, 124(8), 7725-7755.  
938 <https://doi.org/10.1029/2018JB016461>

939 Jamtveit, B., Dunkel, K. G., Petley-Ragan, A., Austrheim, H., Corfu, F., & Schmid, D. W.  
940 (2021). Rapid fluid-driven transformation of lower continental crust associated with thrust-  
941 induced shear heating. *Lithos*, 396, 106216. <https://doi.org/10.1016/j.lithos.2021.106216>

942 John, T., & Schenk, V. (2003). Partial eclogitisation of gabbroic rocks in a late  
943 Precambrian subduction zone (Zambia): prograde metamorphism triggered by fluid  
944 infiltration. *Contributions to Mineralogy and Petrology*, 146(2), 174-191.  
945 <https://doi.org/10.1007/s00410-003-0492-8>

946 John, T., & Schenk, V. (2006). Interrelations between intermediate-depth earthquakes and  
947 fluid flow within subducting oceanic plates: Constraints from eclogite facies  
948 pseudotachylytes. *Geology*, 34(7), 557-560. <https://doi.org/10.1130/G22411.1>

949 Johnson, G. K., Flotow, H. E., & O'hare, P. A. G. (1982). Thermodynamic studies of  
950 zeolites: analcime and dehydrated analcime. *American Mineralogist*, 67(7-8), 736-748.

951 Jung, H., Green li, H. W., & Dobrzhinetskaya, L. F. (2004). Intermediate-depth earthquake  
952 faulting by dehydration embrittlement with negative volume change. *Nature*, 428(6982),  
953 545-549. <https://doi.org/10.1038/nature02412>

954 Kaatz, L., Zertani, S., Moulas, E., John, T., Labrousse, L., Schmalholz, S. M., & Andersen,  
955 T. B. (2021). Widening of hydrous shear zones during incipient eclogitization of

956 metastable dry and rigid lower crust—Holsnøy, western Norway. *Tectonics*, 40(3).  
957 <https://doi.org/10.1029/2020TC006572>

958 Kaatz, L., Reynes, J., Hermann, J., & John, T. (2022). How fluid infiltrates dry crustal rocks  
959 during progressive eclogitization and shear zone formation: insights from H<sub>2</sub>O contents in  
960 nominally anhydrous minerals. *Contributions to Mineralogy and Petrology*, 177(7), 1-20.  
961 <https://doi.org/10.1007/s00410-022-01938-1>

962 Kim, K. T., & Burley, B. J. (1971). Phase equilibria in the system NaAlSi<sub>3</sub>O<sub>8</sub>–NaAlSiO<sub>4</sub>–  
963 H<sub>2</sub>O with special emphasis on the stability of analcite. *Canadian Journal of Earth*  
964 *Sciences*, 8(3), 311-337. <https://doi.org/10.1139/e71-033>

965 Kim, K. T., & Burley, B. J. (1971). Phase Equilibria in the System NaAlSi<sub>3</sub>O<sub>8</sub>–NaAlSiO<sub>4</sub>–  
966 H<sub>2</sub>O Up to 15 Kb. A Theoretical Discussion. *Canadian Journal of Earth Sciences*, 8(5),  
967 549-557. <https://doi.org/10.1139/e71-056>

968 Kim, K. T., & Burley, B. J. (1971). The Solubility of Water in Melts in the System  
969 NaAlSi<sub>3</sub>O<sub>8</sub>–NaAlSiO<sub>4</sub>–H<sub>2</sub>O. *Canadian Journal of Earth Sciences*, 8(5), 558-571.  
970 <https://doi.org/10.1139/e71-057>

971 Kim, K. T., & Burley, B. J. (1980). A further study of analcime solid solutions in the system  
972 NaAlSi<sub>3</sub>O<sub>8</sub>–NaAlSiO<sub>4</sub>–H<sub>2</sub>O, with particular note of an analcime phase  
973 transformation. *Mineralogical Magazine*, 43(332), 1035-1045.  
974 [doi:10.1180/minmag.1980.043.332.13](https://doi.org/10.1180/minmag.1980.043.332.13)

975 Kirby, S., Engdahl, R. E., & Denlinger, R. (1996). Intermediate-depth intraslab  
976 earthquakes and arc volcanism as physical expressions of crustal and uppermost mantle  
977 metamorphism in subducting slabs. Washington DC American Geophysical Union  
978 *Geophysical Monograph Series*, 96, 195-214. [10.1029/GM096p0195](https://doi.org/10.1029/GM096p0195)

979 Kiseeva, E. S., Kamenetsky, V. S., Yaxley, G. M., & Shee, S. R. (2017). Mantle melting  
980 versus mantle metasomatism—“The chicken or the egg” dilemma. *Chemical Geology*, 455,  
981 120-130. <https://doi.org/10.1016/j.chemgeo.2016.10.026>

- 982 Kretz, R. (1983). Symbols for rock-forming minerals. *American mineralogist*, 68(1-2), 277-  
983 279.
- 984 Kühn, A., Glodny, J., Austrheim, H., & Råheim, A. (2002). The Caledonian tectono-  
985 metamorphic evolution of the Lindås Nappe: Constraints from U-Pb, Sm-Nd and Rb-Sr  
986 ages of granitoid dykes. *Norwegian Journal of Geology/Norsk Geologisk Forening*, 82(1).
- 987 Labrousse, L., Jolivet, L., Agard, P., Hébert, R., & Andersen, T. B. (2002). Crustal-scale  
988 boudinage and migmatization of gneiss during their exhumation in the UHP province of  
989 western Norway. *Terra Nova*, 14(4), 263-270. [https://doi.org/10.1046/j.1365-  
990 3121.2002.00422.x](https://doi.org/10.1046/j.1365-3121.2002.00422.x)
- 991 Labrousse, L., Prouteau, G., & Ganzhorn, A. C. (2011). Continental exhumation triggered  
992 by partial melting at ultrahigh pressure. *Geology*, 39(12), 1171-1174.  
993 <https://doi.org/10.1130/G32316.1>
- 994 Labrousse, L., Hetényi, G., Raimbourg, H., Jolivet, L., & Andersen, T. B. (2010). Initiation  
995 of crustal-scale thrusts triggered by metamorphic reactions at depth: Insights from a  
996 comparison between the Himalayas and Scandinavian Caledonides. *Tectonics*, 29(5).  
997 <https://doi.org/10.1029/2009TC002602>
- 998 Lang, H. M., & Gilotti, J. A. (2007). Partial melting of metapelites at ultrahigh-pressure  
999 conditions, Greenland Caledonides. *Journal of Metamorphic Geology*, 25(2), 129-147.  
1000 <https://doi.org/10.1111/j.1525-1314.2006.00687.x>
- 1001 Lawrence, R. D. (1970). Stress analysis based on albite twinning of plagioclase  
1002 feldspars. *Geological Society of America Bulletin*, 81(8), 2507-2512.  
1003 [https://doi.org/10.1130/0016-7606\(1970\)81\[2507:SABOAT\]2.0.CO;2](https://doi.org/10.1130/0016-7606(1970)81[2507:SABOAT]2.0.CO;2)
- 1004 Liou, J. G. (1971). Analcime equilibria. *Lithos*, 4(4), 389-402. [https://doi.org/10.1016/0024-  
1005 4937\(71\)90122-8](https://doi.org/10.1016/0024-4937(71)90122-8)
- 1006 Liu, P., Wu, Y., Liu, Q., Zhang, J., Zhang, L., & Jin, Z. (2014). Partial melting of UHP calc-  
1007 gneiss from the Dabie Mountains. *Lithos*, 192, 86-101.

1008 <https://doi.org/10.1016/j.lithos.2014.01.012>

1009 Liu, P., & Massonne, H. J. (2022). High-pressure granulite facies re-equilibration and  
1010 zoisite–biotite dehydration melting during decompression of an ultrahigh-pressure garnet  
1011 clinopyroxenite from the island of Fjørtoft, Norway. *Journal of Metamorphic Geology*.  
1012 <https://doi.org/10.1111/jmg.12649>

1013 Lund, M. G., & Austrheim, H. (2003). High-pressure metamorphism and deep-crustal  
1014 seismicity: evidence from contemporaneous formation of pseudotachylytes and eclogite  
1015 facies coronas. *Tectonophysics*, 372(1-2), 59-83. [https://doi.org/10.1016/S0040-  
1016 1951\(03\)00232-4](https://doi.org/10.1016/S0040-1951(03)00232-4)

1017 Mancktelow, N. S. (2008). Tectonic pressure: Theoretical concepts and modelled  
1018 examples. *Lithos*, 103(1-2), 149-177. <https://doi.org/10.1016/j.lithos.2007.09.013>

1019 Markl, G. (2001). A new type of silicate liquid immiscibility in peralkaline nepheline  
1020 syenites (lujavrites) of the Ilimaussaq complex, South Greenland. *Contributions to  
1021 Mineralogy and Petrology*, 141(4), 458-472. <https://doi.org/10.1007/s004100100252>

1022 Marshall, D. B., & McLaren, A. C. (1977). Deformation mechanisms in experimentally  
1023 deformed plagioclase feldspars. *Physics and chemistry of minerals*, 1(4), 351-370.  
1024 <https://doi.org/10.1007/BF00308845>

1025 Matthey, D., Jackson, D. H., Harris, N. B. W., & Kelley, S. (1994). Isotopic constraints on  
1026 fluid infiltration from an eclogite facies shear zone, Holsenøy, Norway. *Journal of  
1027 Metamorphic Geology*, 12(3), 311-325. [https://doi.org/10.1111/j.1525-  
1028 1314.1994.tb00025.x](https://doi.org/10.1111/j.1525-1314.1994.tb00025.x)

1029 Menegon, L., Piazzolo, S., & Pennacchioni, G. (2011). The effect of Dauphiné twinning on  
1030 plastic strain in quartz. *Contributions to Mineralogy and Petrology*, 161, 635-652.  
1031 <https://doi.org/10.1007/s00410-010-0554-7>

1032 Moore, J., Beinlich, A., Austrheim, H., & Putnis, A. (2019). Stress orientation–dependent  
1033 reactions during metamorphism. *Geology*, 47(2), 151-154.

- 1034 <https://doi.org/10.1130/G45632.1>
- 1035 Moore, J., Beinlich, A., Porter, J. K., Talavera, C., Berndt, J., Piazzolo, S., ... & Putnis, A.  
1036 (2020). Microstructurally controlled trace element (Zr, U–Pb) concentrations in  
1037 metamorphic rutile: an example from the amphibolites of the Bergen Arcs. *Journal of*  
1038 *Metamorphic Geology*, 38(1), 103-127. <https://doi.org/10.1111/jmg.12514>
- 1039 Morgan, G. B., & London, D. (1996). Optimizing the electron microprobe analysis of  
1040 hydrous alkali aluminosilicate glasses. *American Mineralogist*, 81(9-10), 1176-1185.  
1041 <https://doi.org/10.2138/am-1996-9-1016>
- 1042 Morgan, G. B., & London, D. (2005). Effect of current density on the electron microprobe  
1043 analysis of alkali aluminosilicate glasses. *American Mineralogist*, 90(7), 1131-1138.  
1044 <https://doi.org/10.2138/am.2005.1769>
- 1045 Moulas, E., Burg, J. P., & Podladchikov, Y. (2014). Stress field associated with elliptical  
1046 inclusions in a deforming matrix: Mathematical model and implications for tectonic  
1047 overpressure in the lithosphere. *Tectonophysics*, 631, 37-49.  
1048 <https://doi.org/10.1016/j.tecto.2014.05.004>
- 1049 Nasipuri, P., & Bhattacharya, A. (2007). Melt-assisted interior to margin switch from  
1050 dislocation to diffusion creep in coarse grained plagioclase: Evidence from a deformed  
1051 anorthosite pluton. *Journal of Structural Geology*, 29(8), 1327-1338.  
1052 <https://doi.org/10.1016/j.jsg.2007.04.005>
- 1053 Newton, M. S., & Kennedy, G. C. (1968). Jadeite, analcite, nepheline, and albite at high  
1054 temperatures and pressures. *American Journal of Science*, 266(8), 728-735.  
1055 <https://doi.org/10.2475/ajs.266.8.728>
- 1056 Pattison D. R., De Capitani, C., & Gaidies, F. (2011). Petrological consequences of  
1057 variations in metamorphic reaction affinity. *Journal of Metamorphic Geology*, 29(9), 953-  
1058 977. <https://doi.org/10.1111/j.1525-1314.2011.00950.x>
- 1059 Pe-Piper, G., Piper, D. J., & Nagle, J. (2019). Scapolite and analcime: Monitors of

1060 magmatic fluid metasomatism in a major shear zone. *Chemical Geology*, 522, 208-222.  
1061 <https://doi.org/10.1016/j.chemgeo.2019.05.014>

1062 Peters, T., Luth, W. C., & Tuttle, O. F. (1966). The melting of analcite solid solutions in the  
1063 system NaAlSi<sub>3</sub>O<sub>8</sub>-NaAlSi<sub>3</sub>O<sub>8</sub>-H<sub>2</sub>O. *American Mineralogist: Journal of Earth and*  
1064 *Planetary Materials*, 51(5-6), 736-753.

1065 Petley-Ragan, A., Dunkel, K. G., Austrheim, H., Ildefonse, B., & Jamtveit, B. (2018).  
1066 Microstructural records of earthquakes in the lower crust and associated fluid-driven  
1067 metamorphism in plagioclase-rich granulites. *Journal of Geophysical Research: Solid*  
1068 *Earth*, 123(5), 3729-3746. <https://doi.org/10.1029/2017JB015348>

1069 Petley-Ragan, A., Ben-Zion, Y., Austrheim, H., Ildefonse, B., Renard, F., & Jamtveit, B.  
1070 (2019). Dynamic earthquake rupture in the lower crust. *Science Advances*, 5(7),  
1071 eaaw0913. DOI: [10.1126/sciadv.aaw0913](https://doi.org/10.1126/sciadv.aaw0913)

1072 Putnis, A., & Austrheim, H. (2010). Fluid-induced processes: metasomatism and  
1073 metamorphism. *Geofluids*, 10(1-2), 254-269. [https://doi.org/10.1111/j.1468-](https://doi.org/10.1111/j.1468-8123.2010.00285.x)  
1074 [8123.2010.00285.x](https://doi.org/10.1111/j.1468-8123.2010.00285.x)

1075 Putnis, A., Jamtveit, B., & Austrheim, H. (2017). Metamorphic processes and seismicity:  
1076 the Bergen Arcs as a natural laboratory. *Journal of Petrology*, 58(10), 1871-1898.  
1077 <https://doi.org/10.1093/petrology/egx076>

1078 Putnis, A., Moore, J., Prent, A. M., Beinlich, A., & Austrheim, H. (2021). Preservation of  
1079 granulite in a partially eclogitized terrane: Metastable phenomena or local pressure  
1080 variations?. *Lithos*, 400, 106413. <https://doi.org/10.1016/j.lithos.2021.106413>

1081 Raimbourg, H. (2005). Mécanismes d'éclogitisation et conséquences mécaniques pour  
1082 l'exhumation des roches métamorphiques de haute pression (Doctoral dissertation,  
1083 Université Pierre et Marie Curie-Paris VI).

1084 Raimbourg, H., Jolivet, L., Labrousse, L., Leroy, Y., & Avigad, D. (2005). Kinematics of  
1085 syneclogite deformation in the Bergen Arcs, Norway: implications for exhumation

1086 mechanisms. Geological Society, London, Special Publications, 243(1), 175-192.  
1087 <https://doi.org/10.1144/GSL.SP.2005.243.01.13>

1088 Raimbourg, H., Goffé, B., & Jolivet, L. (2007). Garnet reequilibration and growth in the  
1089 eclogite facies and geodynamical evolution near peak metamorphic  
1090 conditions. Contributions to Mineralogy and Petrology, 153(1), 1-28.  
1091 <https://doi.org/10.1007/s00410-006-0130-3>

1092 Roberts, D. (2003). The Scandinavian Caledonides: event chronology, palaeogeographic  
1093 settings and likely modern analogues. Tectonophysics, 365(1-4), 283-299.  
1094 [https://doi.org/10.1016/S0040-1951\(03\)00026-X](https://doi.org/10.1016/S0040-1951(03)00026-X)

1095 Rosenberg, C. L., & Handy, M. R. (2001). Mechanisms and orientation of melt segregation  
1096 paths during pure shearing of a partially molten rock analog (norcamphor-  
1097 benzamide). Journal of Structural Geology, 23(12), 1917-1932.  
1098 [https://doi.org/10.1016/S0191-8141\(01\)00037-2](https://doi.org/10.1016/S0191-8141(01)00037-2)

1099 Rosenberg, C. L., & Handy, M. R. (2005). Experimental deformation of partially melted  
1100 granite revisited: implications for the continental crust. Journal of metamorphic  
1101 Geology, 23(1), 19-28. <https://doi.org/10.1111/j.1525-1314.2005.00555.x>

1102 Roux, J., & Hamilton, D. L. (1976). Primary igneous analcite—an experimental  
1103 study. Journal of Petrology, 17(2), 244-257. <https://doi.org/10.1093/petrology/17.2.244>

1104 Rubie, D. C. (1986). The catalysis of mineral reactions by water and restrictions on the  
1105 presence of aqueous fluid during metamorphism. Mineralogical Magazine, 50(357), 399-  
1106 415. [doi:10.1180/minmag.1986.050.357.05](https://doi.org/10.1180/minmag.1986.050.357.05)

1107 Rubie, D. C. (1998). Disequilibrium during metamorphism: the role of nucleation  
1108 kinetics. Geological Society, London, Special Publications, 138(1), 199-214.  
1109 <https://doi.org/10.1144/GSL.SP.1996.138.01.12>

1110 Scambelluri, M., Pennacchioni, G., Gilio, M., Bestmann, M., Plümpner, O., & Nestola, F.  
1111 (2017). Fossil intermediate-depth earthquakes in subducting slabs linked to differential

1112 stress release. *Nature Geoscience*, 10(12), 960-966. [https://doi.org/10.1038/s41561-017-](https://doi.org/10.1038/s41561-017-0010-7)  
1113 [0010-7](https://doi.org/10.1038/s41561-017-0010-7)

1114 Schmidt, M. W., & Poli, S. (2004). Magmatic epidote. *Reviews in Mineralogy and*  
1115 *Geochemistry*, 56(1), 399-430. <https://doi.org/10.2138/gsrmg.56.1.399>

1116 Schneider, J., Bosch, D., Monie, P., & Bruguier, O. (2007). Micro-scale element migration  
1117 during eclogitisation in the Bergen arcs (Norway): a case study on the role of fluids and  
1118 deformation. *Lithos*, 96(3-4), 325-352. <https://doi.org/10.1016/j.lithos.2006.10.001>

1119 Schorn, S., & Diener, J. F. A. (2017). Details of the gabbro-to-eclogite transition  
1120 determined from microtextures and calculated chemical potential relationships. *Journal of*  
1121 *Metamorphic Geology*, 35(1), 55-75. <https://doi.org/10.1111/jmg.12220>

1122 Shi, F., Wang, Y., Yu, T., Zhu, L., Zhang, J., Wen, J., ... & Jin, Z. (2018). Lower-crustal  
1123 earthquakes in southern Tibet are linked to eclogitization of dry metastable  
1124 granulite. *Nature communications*, 9(1), 1-13. [https://doi.org/10.1038/s41467-018-05964-](https://doi.org/10.1038/s41467-018-05964-1)  
1125 [1](https://doi.org/10.1038/s41467-018-05964-1)

1126 Skjerlie, K. P., & Patiño Douce, A. E. (2002). The fluid-absent partial melting of a zoisite-  
1127 bearing quartz eclogite from 1· 0 to 3· 2 GPa; Implications for melting in thickened  
1128 continental crust and for subduction-zone processes. *Journal of Petrology*, 43(2), 291-  
1129 314. <https://doi.org/10.1093/petrology/43.2.291>

1130 Smith, J. V., & Brown, W. L. (1988). Twins. In *Feldspar Minerals* (pp. 519-554). Springer,  
1131 Berlin, Heidelberg. [https://doi.org/10.1007/978-3-642-72594-4\\_18](https://doi.org/10.1007/978-3-642-72594-4_18)

1132 Steltenpohl, M. G., Kassos, G., & Andresen, A. (2006). Retrograded eclogite-facies  
1133 pseudotachylytes as deep-crustal paleoseismic faults within continental basement of  
1134 Lofoten, north Norway. *Geosphere*, 2(1), 61-72. <https://doi.org/10.1130/GES00035.1>

1135 Sternlof, K. R., Rudnicki, J. W., & Pollard, D. D. (2005). Anticrack inclusion model for  
1136 compaction bands in sandstone. *Journal of Geophysical Research: Solid Earth*, 110(B11).  
1137 <https://doi.org/10.1029/2005JB003764>

- 1138 Stünitz, H., & Tullis, J. (2001). Weakening and strain localization produced by syn-  
1139 deformational reaction of plagioclase. *International Journal of Earth Sciences*, 90(1), 136-  
1140 148. <https://doi.org/10.1007/s005310000148>
- 1141 Thompson, A. B. (1973). Analcime: Free energy from hydrothermal data. Implications for  
1142 phase equilibria and thermodynamic quantities for phases in NaAlO<sub>2</sub>-SiO<sub>2</sub>-  
1143 H<sub>2</sub>O. *American Mineralogist: Journal of Earth and Planetary Materials*, 58(3-4\_Part\_1),  
1144 277-286.
- 1145 Tsuchiyama, A., & Takahashi, E. (1983). Melting kinetics of a plagioclase  
1146 feldspar. *Contributions to Mineralogy and Petrology*, 84(4), 345-354.  
1147 <https://doi.org/10.1007/BF01160286>
- 1148 Tsujimori, T., & Harlow, G. E. (2012). Petrogenetic relationships between jadeitite and  
1149 associated high-pressure and low-temperature metamorphic rocks in worldwide jadeitite  
1150 localities: a review. *European Journal of Mineralogy*, 24(2), 371-390.  
1151 <https://doi.org/10.1127/0935-1221/2012/0024-2193>
- 1152 Vanderhaeghe, O. (2009). Migmatites, granites and orogeny: Flow modes of partially-  
1153 molten rocks and magmas associated with melt/solid segregation in orogenic  
1154 belts. *Tectonophysics*, 477(3-4), 119-134. <https://doi.org/10.1016/j.tecto.2009.06.021>
- 1155 Velde, B., & Besson, J. M. (1981). Raman spectra of analcime under  
1156 pressure. *Physics and Chemistry of Minerals*, 7(2), 96-99.  
1157 <https://doi.org/10.1007/BF00309459>
- 1158 Vernon, R. H. (2011). Microstructures of melt-bearing regional metamorphic  
1159 rocks. *Geological Society of America Memoirs*, 207, 1-11.
- 1160 Wain, A. L., Waters, D. J., & Austrheim, H. (2001). Metastability of granulites and  
1161 processes of eclogitisation in the UHP region of western Norway. *Journal of Metamorphic  
1162 Geology*, 19(5), 609-625. <https://doi.org/10.1046/j.0263-4929.2001.00333.x>
- 1163 Wayte, G. J., Worden, R. H., Rubie, D. C., & Droop, G. T. (1989). A TEM study of

- 1164 disequilibrium plagioclase breakdown at high pressure: the role of infiltrating  
1165 fluid. *Contributions to Mineralogy and Petrology*, 101(4), 426-437.  
1166 <https://doi.org/10.1007/BF00372216>
- 1167 Wenk, H. R., Joswig, W., Tagai, T., Korekawa, M., & Smith, B. K. (1980). The average  
1168 structure of An 62–66 labradorite. *American Mineralogist*, 65(1-2), 81-95.
- 1169 Wang, L., Kusky, T. M., Polat, A., Wang, S., Jiang, X., Zong, K., ... & Fu, J. (2014). Partial  
1170 melting of deeply subducted eclogite from the Sulu orogen in China. *Nature*  
1171 *communications*, 5(1), 1-11. <https://doi.org/10.1038/ncomms6604>
- 1172 White, R. W., Powell, R., & Holland, T. J. B. (2001). Calculation of partial melting equilibria  
1173 in the system Na<sub>2</sub>O–CaO–K<sub>2</sub>O–FeO–MgO–Al<sub>2</sub>O<sub>3</sub>–SiO<sub>2</sub>–H<sub>2</sub>O (NCKFMASH). *Journal of*  
1174 *metamorphic Geology*, 19(2), 139-153. <https://doi.org/10.1046/j.0263-4929.2000.00303.x>
- 1175 White, R. W., Powell, R. O. G. E. R., Holland, T. J. B., Johnson, T. E., & Green, E. C. R.  
1176 (2014). New mineral activity–composition relations for thermodynamic calculations in  
1177 metapelitic systems. *Journal of Metamorphic Geology*, 32(3), 261-286.  
1178 <https://doi.org/10.1111/jmg.12071>
- 1179 Yamato, P., Duret, T., Baïssat, M., & Luisier, C. (2022). Reaction-induced volume  
1180 change triggers brittle failure at eclogite facies conditions. *Earth and Planetary Science*  
1181 *Letters*, 584, 117520. <https://doi.org/10.1016/j.epsl.2022.117520>
- 1182 Young, D. J., & Kylander-Clark, A. R. C. (2015). Does continental crust transform during  
1183 eclogite facies metamorphism?. *Journal of Metamorphic Geology*, 33(4), 331-  
1184 357. <https://doi.org/10.1111/jmg.12123>
- 1185 Zertani, S., John, T., Tilmann, F., Motra, H. B., Keppler, R., Andersen, T. B., & Labrousse,  
1186 L. (2019). Modification of the seismic properties of subducting continental crust by  
1187 eclogitization and deformation processes. *Journal of Geophysical Research: Solid*  
1188 *Earth*, 124(9), 9731-9754. <https://doi.org/10.1029/2019JB017741>
- 1189 Zertani, S., John, T., Brachmann, C., Vrijmoed, J. C., & Plümpner, O. (2022). Reactive fluid

1190 flow guided by grain-scale equilibrium reactions during eclogitization of dry crustal  
1191 rocks. Contributions to Mineralogy and Petrology, 177(6), 1-18.  
1192 <https://doi.org/10.1007/s00410-022-01928-3>

1193 Zhong, X., Petley-Ragan, A. J., Incel, S. H., Dabrowski, M., Andersen, N. H., & Jamtveit,  
1194 B. (2021). Lower crustal earthquake associated with highly pressurized frictional  
1195 melts. Nature Geoscience, 14(7), 519-525. <https://doi.org/10.1038/s41561-021-00760-x>

## 1196 **Figure captions**

1197 **Fig.1 Sample location.** **a** Geological map of northern Holsnøy, Norway, modified from  
1198 Bras et al. (2021) after Austrheim et al. (2013) and Zertani et al. (2019). Red star: location  
1199 of the outcrop studied. **b** Lithological map of the outcrop studied. The blue rectangle  
1200 corresponds to photograph displayed in **c**. **c** Field photograph of the eclogite finger  
1201 sampled. **d** Detailed field photograph of the finger (enlargement from **c**). Blue rectangles:  
1202 location of the thin sections. T1 and T2 black rectangles: studied transects presented in  
1203 Figure 2 and Figure S1

1204 **Fig.2 Ongoing eclogitization through the finger.** BSE images (**a,c-e**) and  
1205 photomicrograph in plane-polarized polarized light (**b**) of transect T1 (see location in  
1206 Fig.1d). Red zones in (**b**): corona structures that define the granulitic foliation. Orange  
1207 arrows: plagioclase-plagioclase grain boundaries in low transformed areas. White arrows:  
1208 analcime-kyanite decorated grain boundaries. Yellow arrows: analcime-bearing injectite  
1209 vein. Green arrows: intersection of kyanite-bearing ferromagnesian rims and analcime-  
1210 kyanite decorated plagioclase grain boundaries. Red arrows: fractures inside garnet. BSE  
1211 image (**e**) is localized in Figure S1a

1212 **Fig.3 Successive textures at grain boundaries.** BSE images illustrating plagioclase-  
1213 plagioclase grain boundaries (**a-c**) and plagioclase-garnet grain boundaries (**d-f**). (**f**) minor  
1214 retrogression of omphacite into a fine-grained symplectite (s)

1215 **Fig.4 Evolution of plagioclase twinning.** Cross-polarized microphotographs of  
1216 plagioclase twins through the transect. (a) Growth twins in preserved granulite (b)

1217 mechanical twins in a partially reacted area, and (c) lack of twins in the final recrystallized  
1218 plagioclase.

1219 **Fig.5 Plagioclase twinning systems: principle and application.** 3D representation of  
1220 the albite **(a)** and of the pericline **(b)** twin systems. R: rhombic section. **(c)** Color plot of  
1221 the Schmid factor (SF) with geometric elements of albite (red symbols) and pericline (light  
1222 blue symbols) twin systems represented. Inset: corresponding focal mechanism-like  
1223 «beachball». **(d)** Map of misorientation angle of a plagioclase grain in a partially  
1224 transformed zone of the finger. **(e)** Orientation map of the same area as in **(d)** plotted with  
1225 a colormap (inset) corresponding to the angle between X direction, here defined as  
1226 parallel to the [100] direction, and the thin section plane. Y perpendicular to the plane  
1227 (010). Blue: untwinned, green: twinned, red contours: twin boundaries. **(f)** Stereogram of  
1228 twins in the plagioclase crystal from **(d)**. Inset: corresponding focal mechanism-like  
1229 «beachball»

1230 **Fig.6** BSE image of the low transformed area of transect T1, showing location of grains  
1231 where focal mechanism-like «beachballs» have been extracted. **(b)** Stacked «beachballs»  
1232 of plagioclase grains indicated in **(a)**. **(c)** Spherical functions of stacked and averaged  
1233 Schmid factor

1234 **Fig.7 Twinning and reaction induced grain size reduction of plagioclase.** **(a)**  
1235 Orientation map of a former plagioclase grain from a reacted area (see location in Fig.  
1236 6a), plotted with a colormap (inset) corresponding to the angle between X direction, here  
1237 defined as parallel to the [100] direction, and the thin section plane. Y perpendicular to the  
1238 plane (010). **(b)** Grain size histogram of “grains” delimited by grain- and twin- boundaries.  
1239 **(c)** Enlargement showing grain size reduction induced by zoisite formation and twinning.  
1240 Twin boundaries are indicated in red and low angle grain boundaries in white.

1241 **Fig.8 Chronological and textural relations in analcime-bearing grain boundaries.**  
1242 N020 orientation in **(b)** is valid for all other panels of this figure. Red arrow in **(b)**: hole  
1243 created by the EPMA electron beam. Red arrow in **(c)**: porosity in an analcime pool. Red  
1244 arrow in **(e)**: intersection of kyanite-bearing ferromagnesian rims and analcime-kyanite  
1245 decorated plagioclase grain boundaries

1246 **Fig.9 Raman spectrum of analcime.** Characteristic peaks are indicated in green. Inset:  
1247 water peaks of the mineral

1248 **Fig.10 Plagioclase grain size reduction in a kyanite-analcime-bearing grain**  
1249 **boundary.** BSE image (a): location of the EBSD phase map (d), and additional details  
1250 (b,c). Red arrows: low dihedral angles of the analcime pools toward re-crystallized  
1251 plagioclase grains. (e) Grain size distribution of plagioclase and kyanite grains from the  
1252 EBSD map shown in (d)

1253 **Fig.11  $P$ - $T$  pseudosections at  $X_{H_2O} = 1$  wt % (left) and  $P$ - $X_{H_2O}$  pseudosections at  $T =$**   
1254 **700°C (right).** Chemical composition used to performed the calculations (listed in Table  
1255 3) are, from top to bottom: the initial granulitic plagioclase composition and the albitized  
1256 plagioclase composition (Fig.2d). Calculations have been performed using the melt  
1257 solution model of Green et al. (2016), see Method section for details. Melt modes (in  
1258 volume %) are indicated by the red lines, and  $X_{An}$  by the yellow lines. Zones where melt  
1259 is predicted are highlighted in red.

1260 **Fig.12 Finger Propagation.** Pressure field evolution at the tip of a reacting and  
1261 propagating finger (modified from Yamato et al., 2022).  $\Delta P$  corresponds to variation of  
1262 pressure  $P$  relative to background pressure  $P_{bg}$  such as  $\Delta P = (P - P_{bg}) / P$

## 1263 Table captions

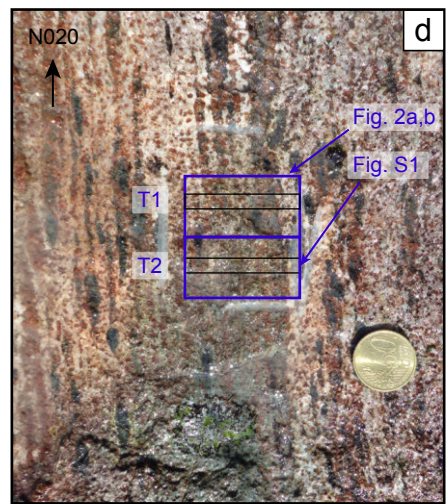
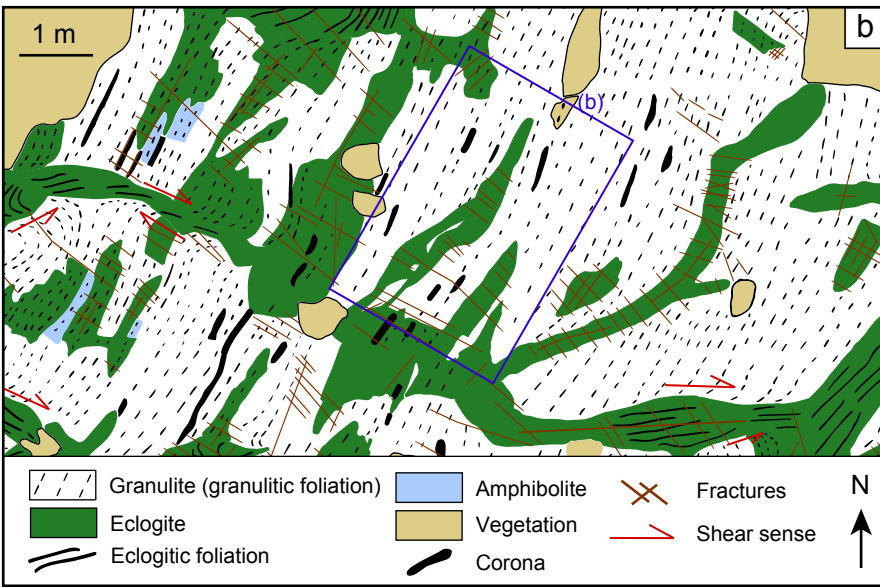
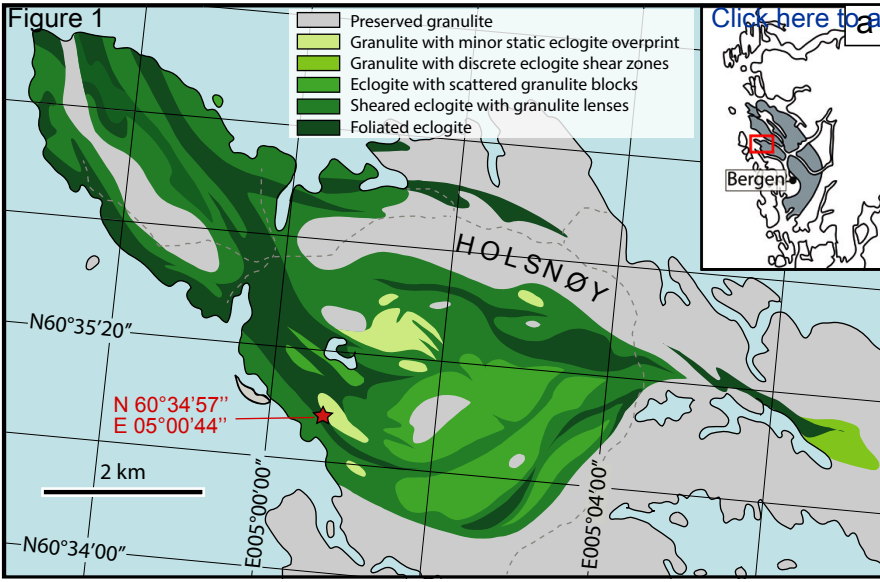
1264 **Table 1** Representative mineral composition (wt%) of granulite to eclogite parageneses.  
1265 Composition of granulite-facies minerals results from analyses in the core of the grains,  
1266 while analyses in minerals from the partially-transformed area have been performed at  
1267 grain rims. The structural formulae of plagioclase, garnet and pyroxene were calculated  
1268 based on 8 oxygens, 12 oxygens and 6 oxygens, respectively. b.d.l = below detection  
1269 limit. n.a = not analysed. All Fe is counted as Fe<sup>2+</sup>

1270 **Table 2** Representative mineral composition (wt%) of analcime, matrix plagioclase, and  
1271 plagioclase around kyanite in analcime-kyanite grain boundaries. The structural formulae  
1272 of plagioclase were calculated based on 8 oxygens. b.d.l = below detection limit. n.a = not

1273 analysed

1274 **Table 3** Chemical compositions (wt%) used for thermodynamic calculations. Analyses for  
1275 the whole rock composition were performed at ALS Dublin (OMAC Laboratories) by ICP-  
1276 AES (major elements) and ICP-MS (trace elements). Loss on Ignition (LOI)  
1277 measurements indicate a value of 0.29 wt%. The whole rock composition given here was  
1278 recalculated considering 0 wt% H<sub>2</sub>O for a total of 100 wt% oxides.

1279



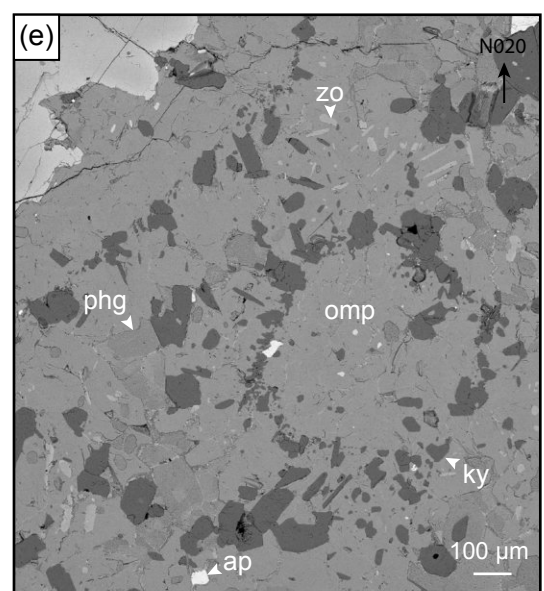
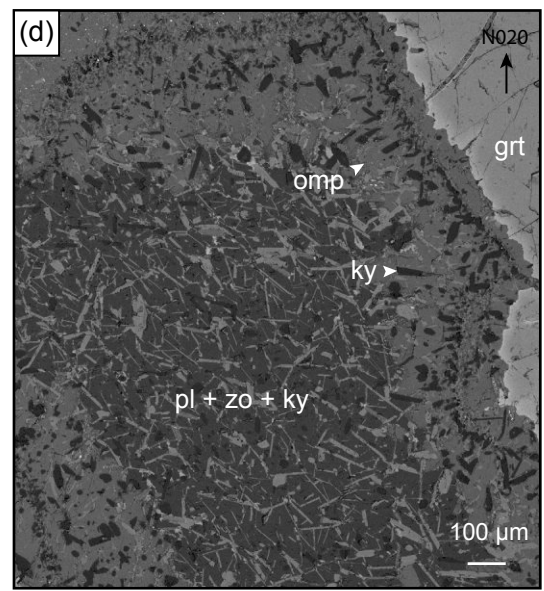
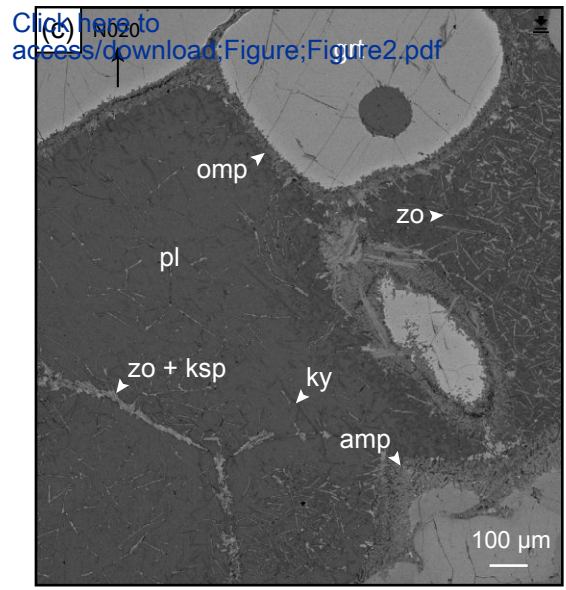
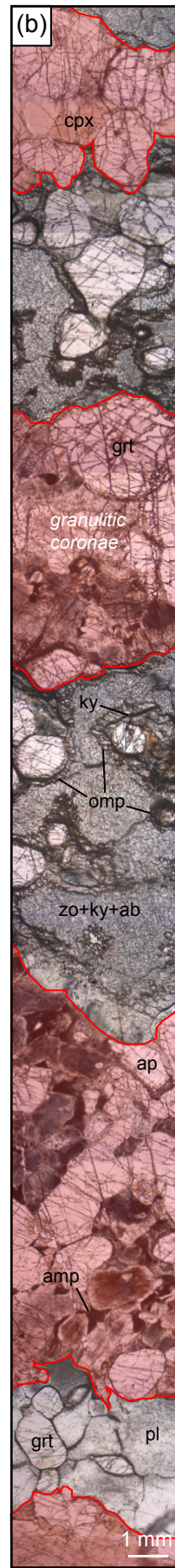
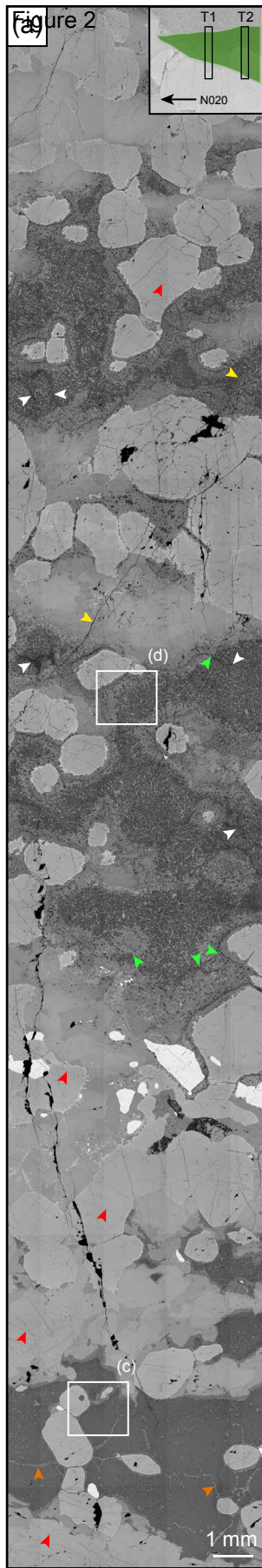
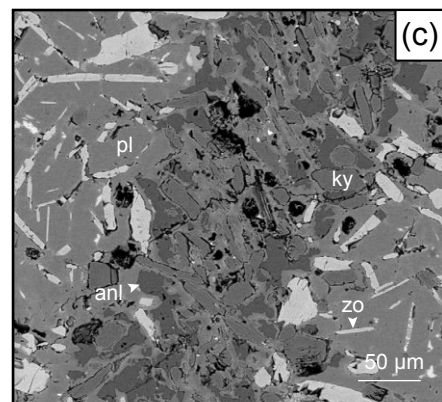
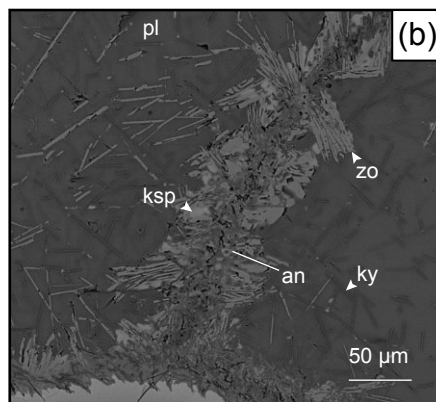
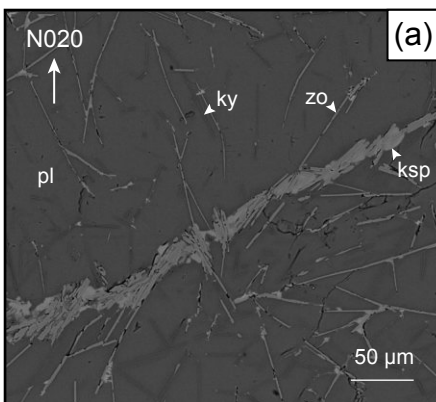
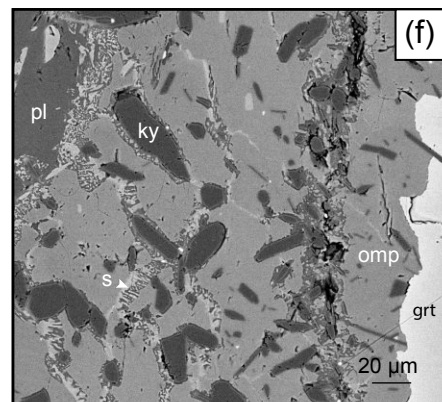
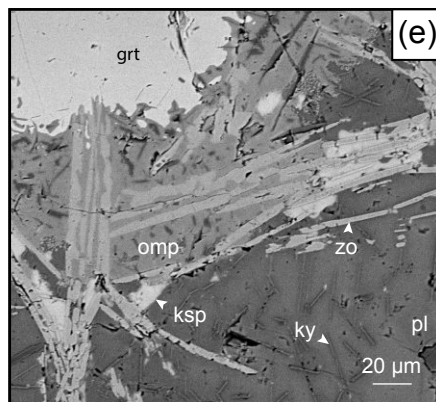
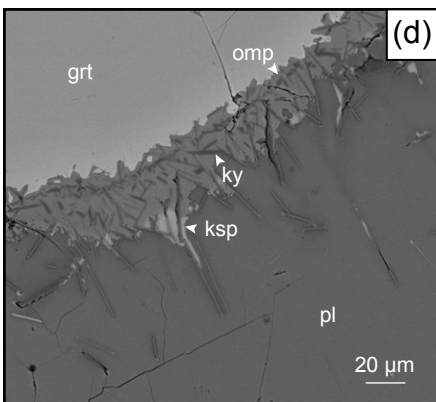


**Figure 3 PI grain boundaries**

[Click here to access/download;Figure;Figure3.pdf](#)

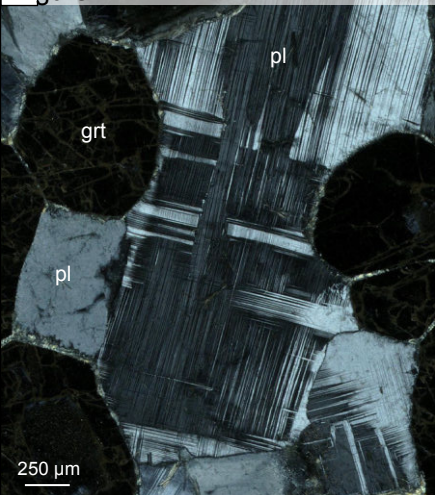


**PI - Grt grain boundaries**

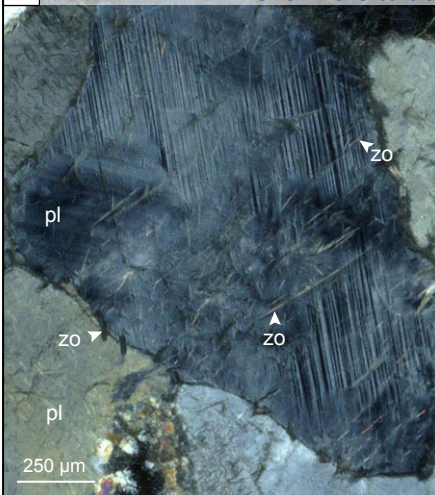


→  
*Increasing reaction extent*

(a) Growth twins - preserved plagioclase



(b) Mechanical twins - reacting plagioclase



(c) No twins - recrystallized plagioclase

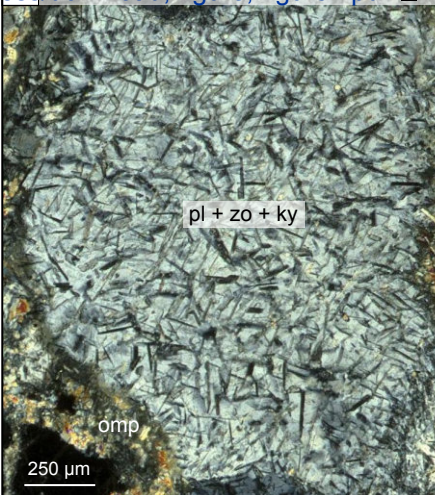
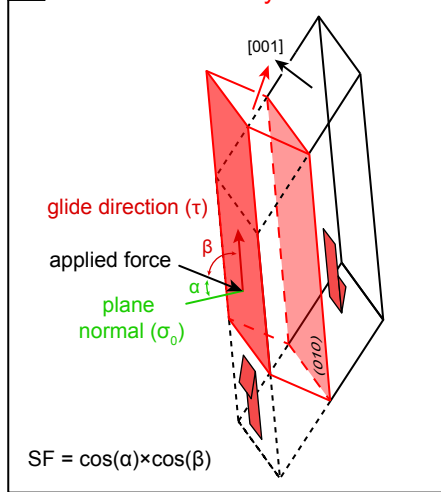
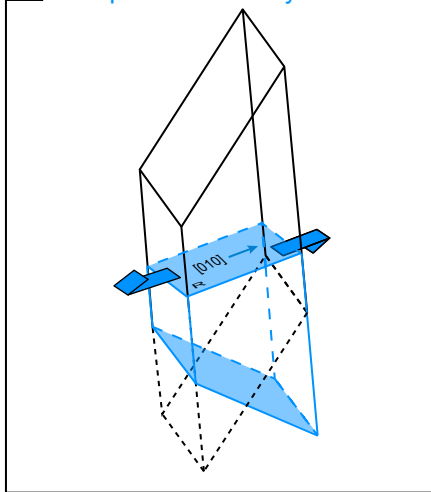


Figure 5 **albite twin system**



(b) **pericline twin system**



Click here to access/download;Figure;Figure5.pdf

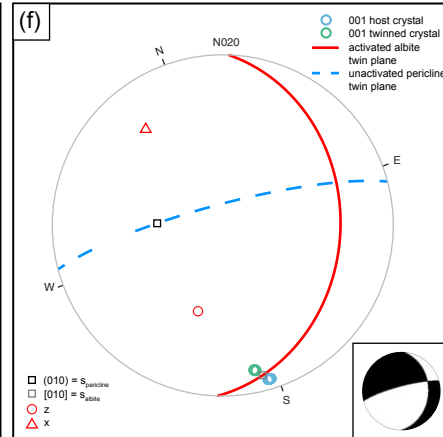
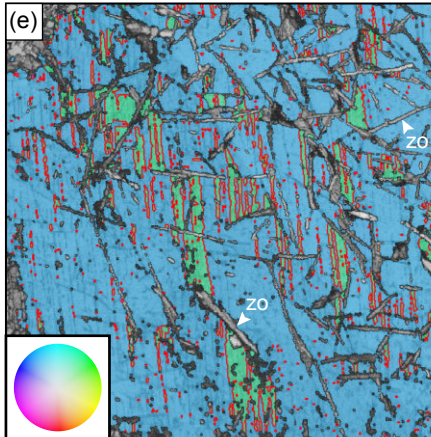
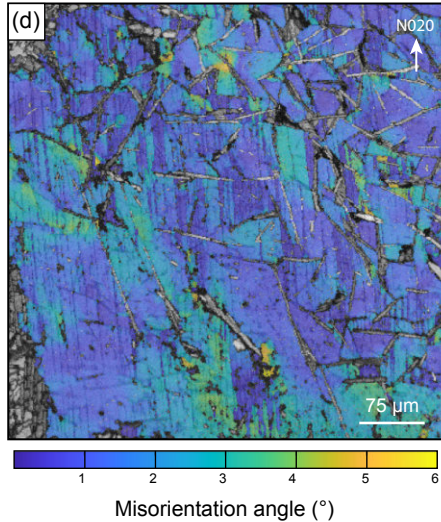
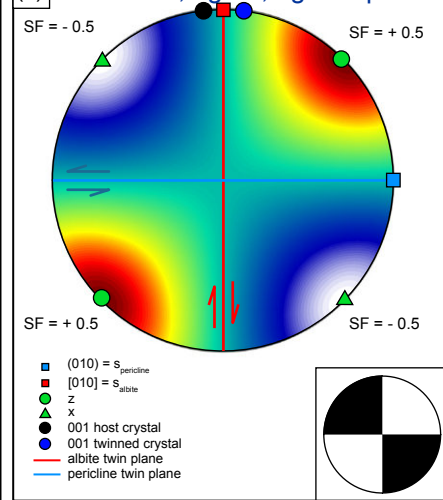
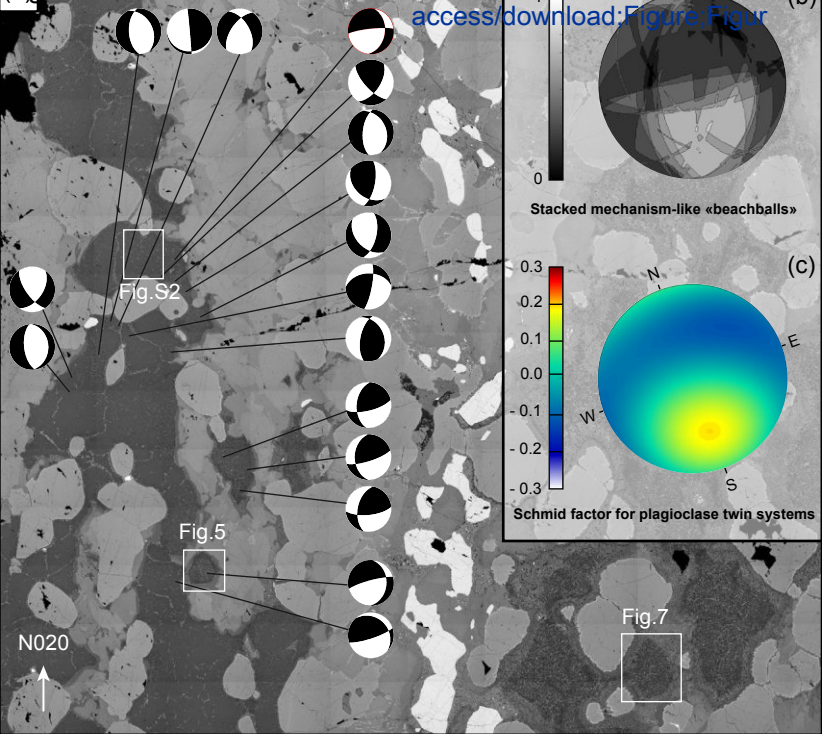
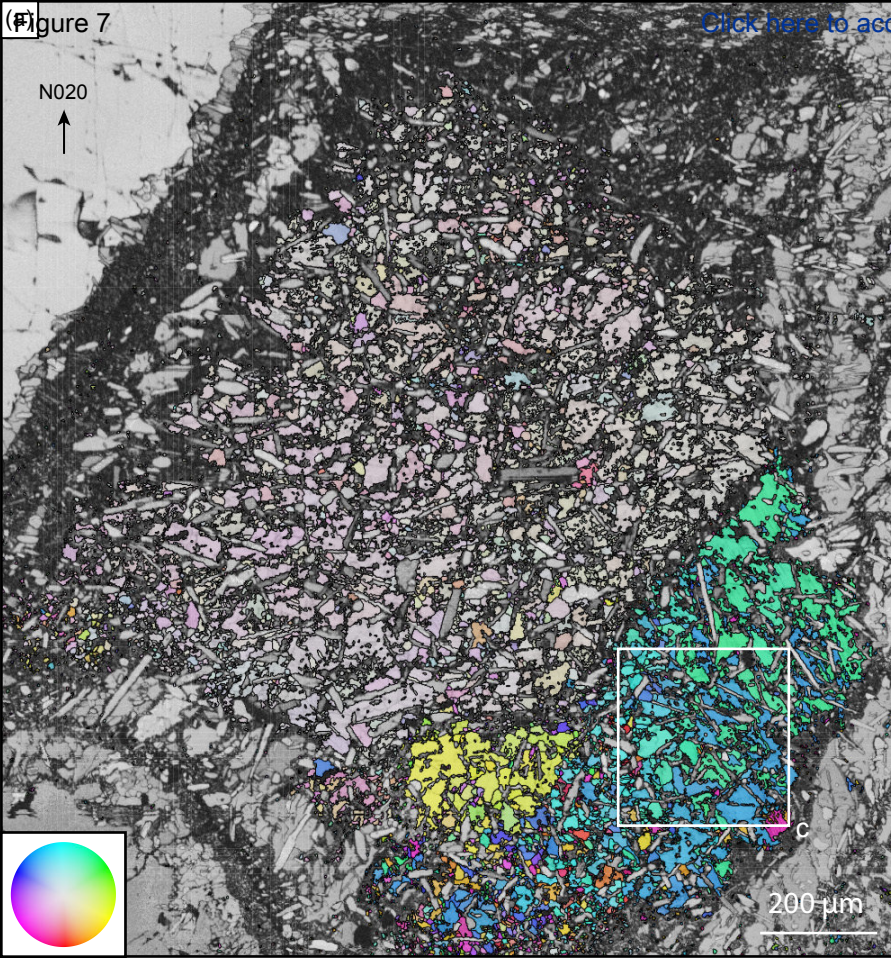


Figure 6

[Click here to access/download:Figure:Figure](#)



(a) Figure 7



[Click here to access/download;Figure;Figure7.pdf](#) (b)

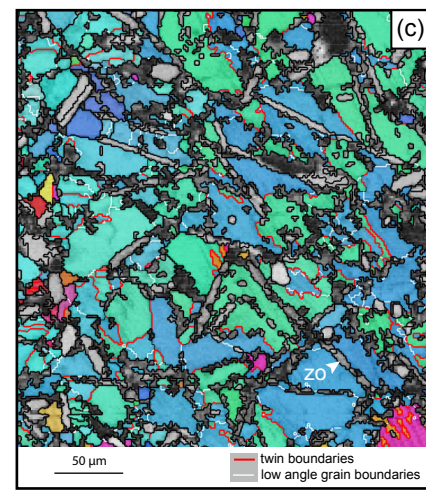
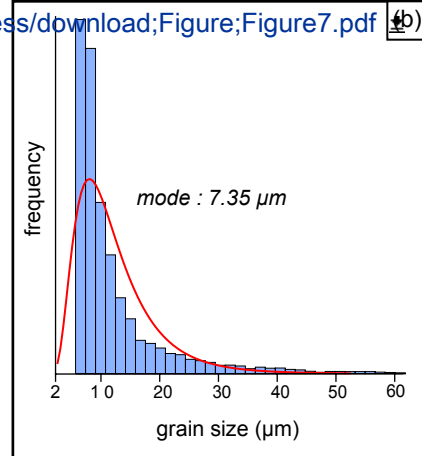
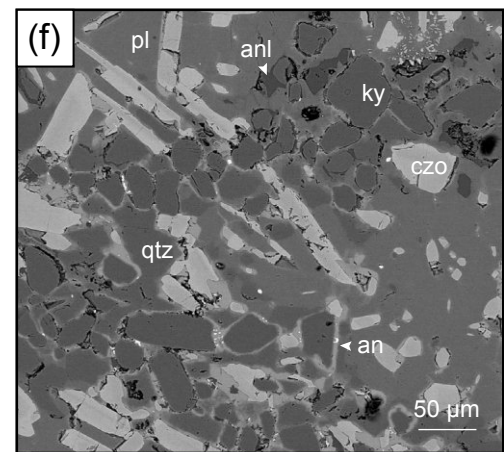
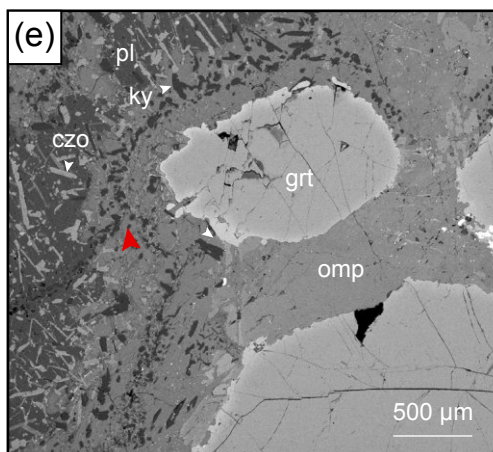
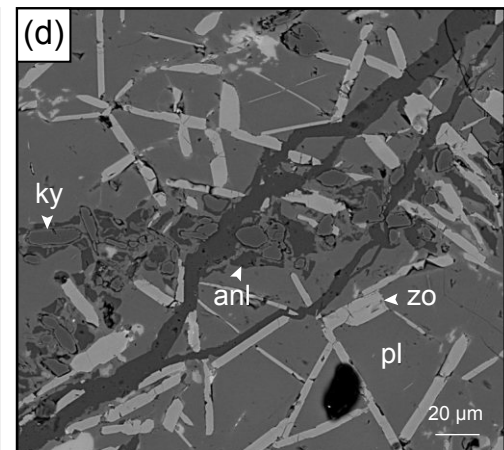
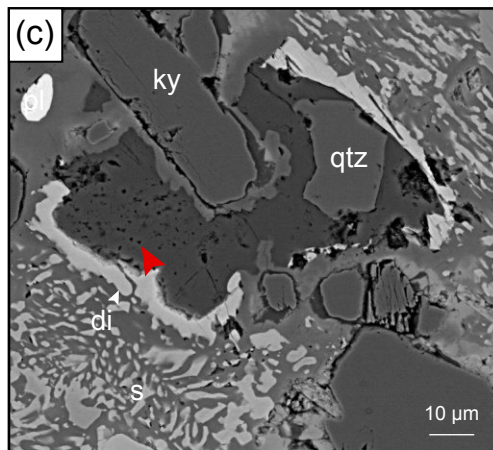
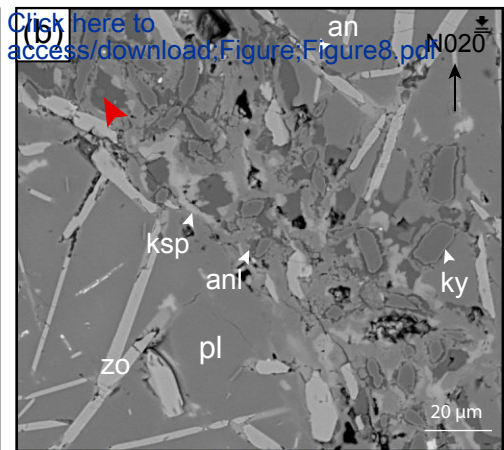
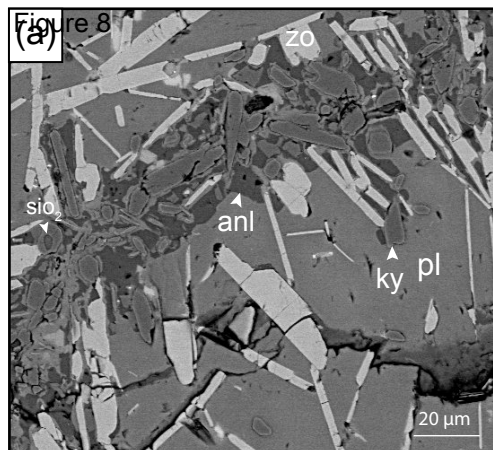


Figure 8



Click here to access/download:Figure:Figure8.pdf

Figure 9

482

[Click here to access/download;Figur](#)



Normalized intensity

297 390

3625

3558

3350

3800

1102

300

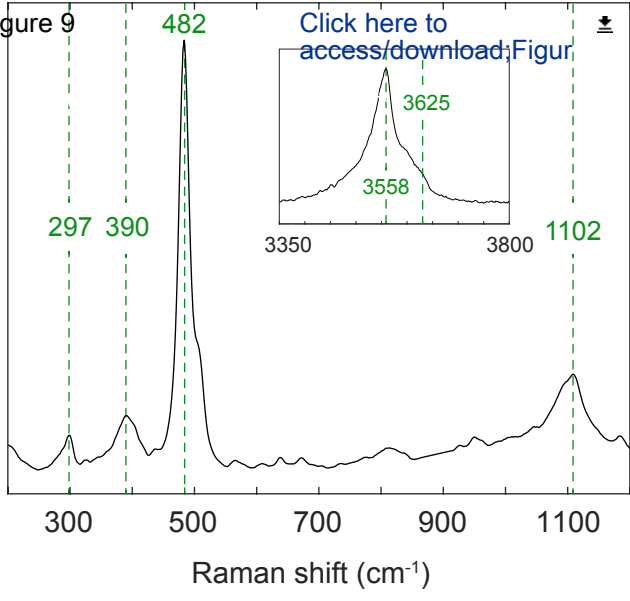
500

700

900

1100

Raman shift ( $\text{cm}^{-1}$ )



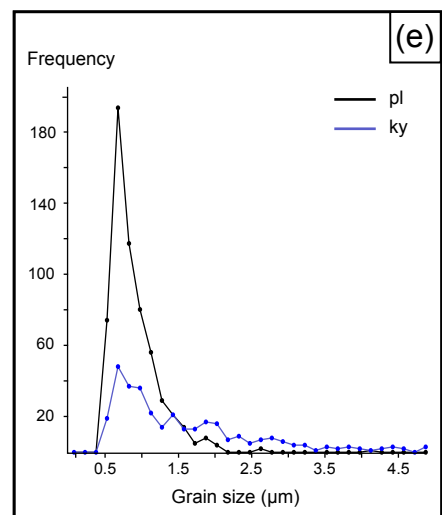
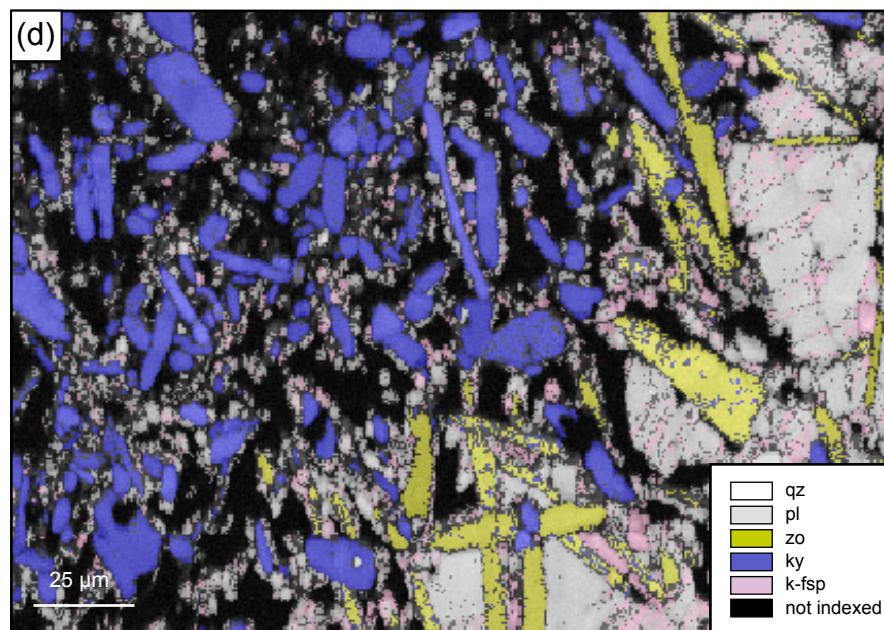
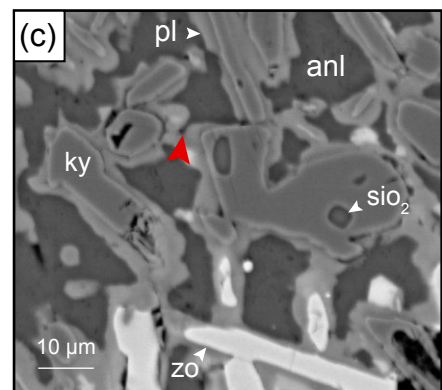
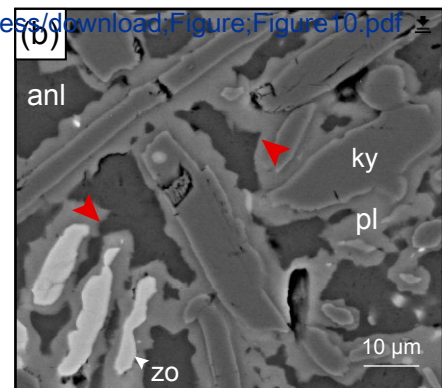
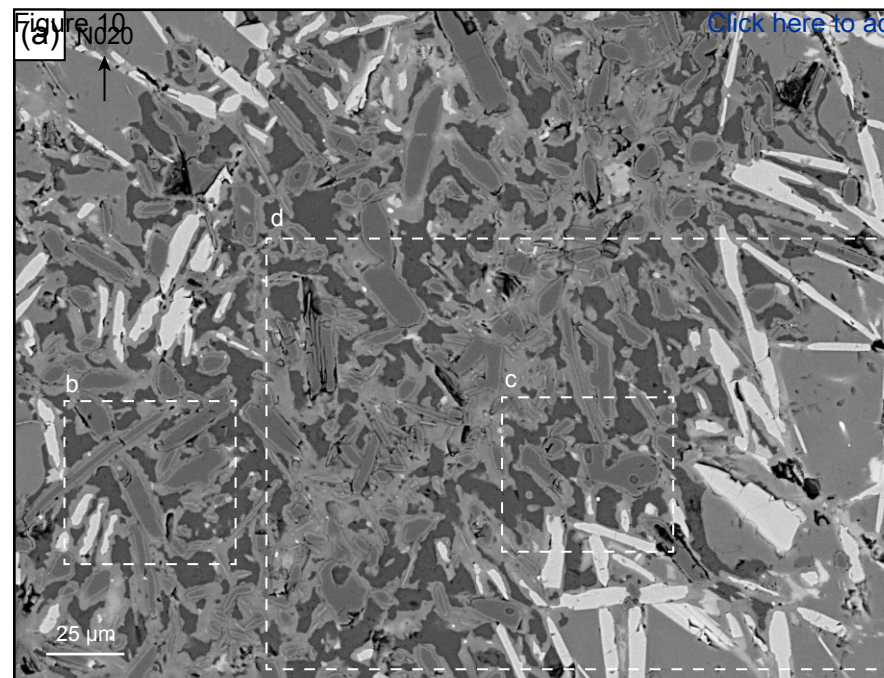
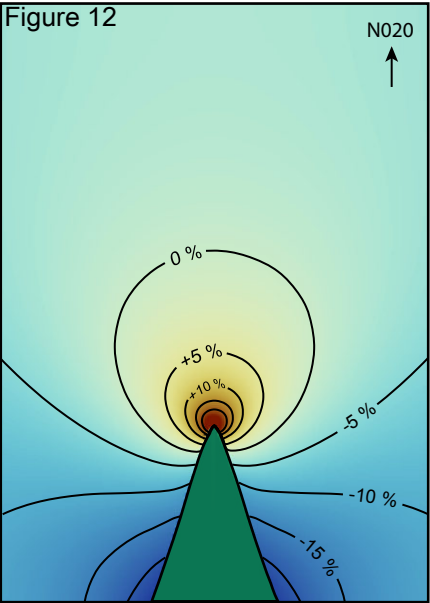




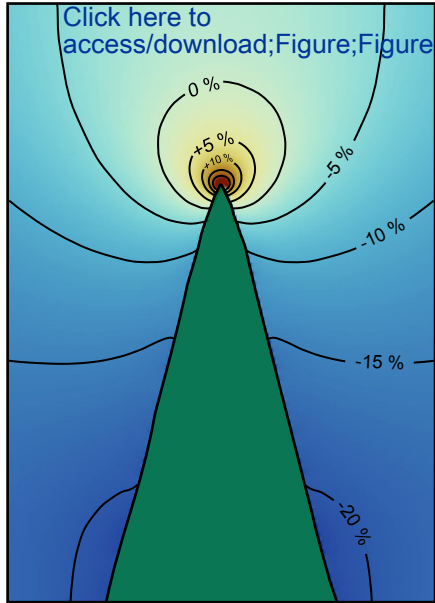
Figure 12

N020  
↑

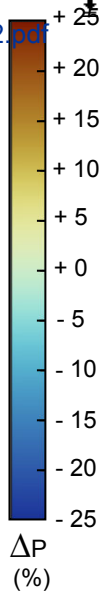


$t_1$

[Click here to access/download;Figure;Figure12.pdf](#)



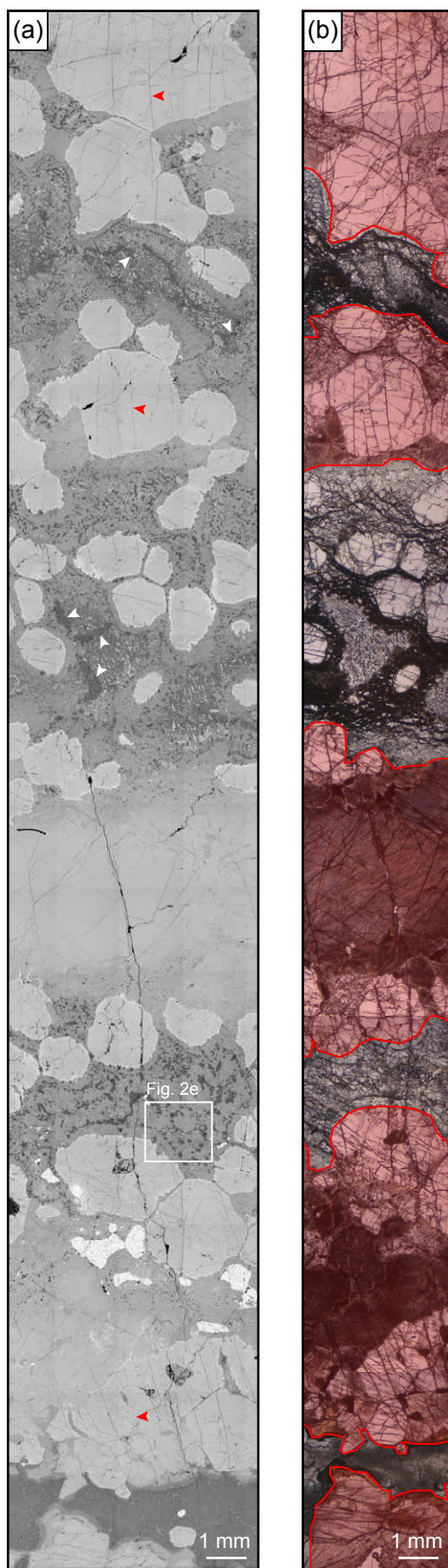
$t_2$



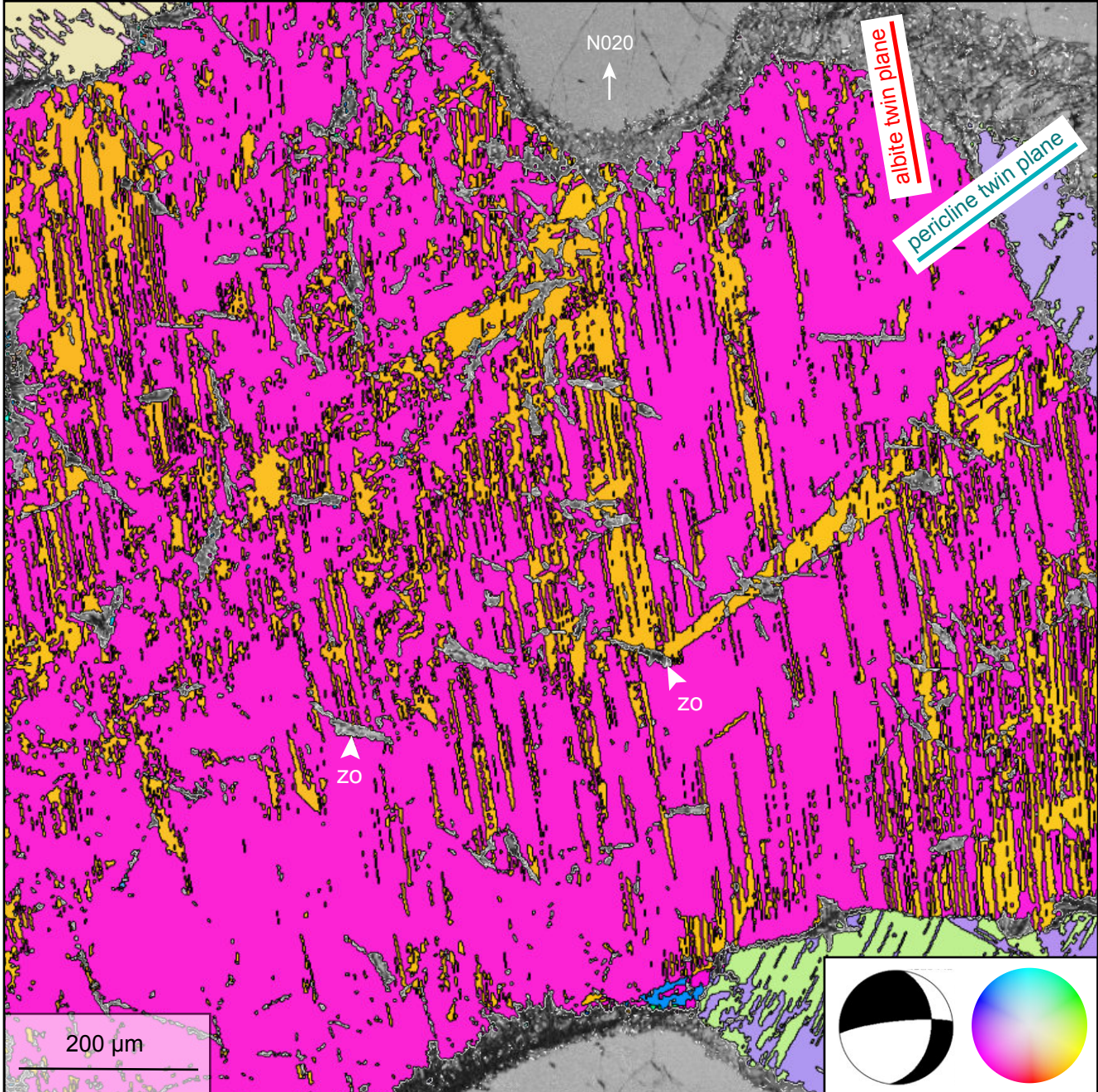
Paragenesis Mineral	Granulite (as in Figure 2c)				Partially eclogitized (as in Figure 2d)			
	Plagioclase	Garnet	Pyroxene	Amphibole	Plagioclase rim	Clinozoisite	Garnet rim	Pyroxene rim
Number of analysis	4	10	9	4	12	16	8	3
SiO <sub>2</sub>	58.3	41.3	46.8	41.2	64.5	39.2	36.4	55.7
TiO <sub>2</sub>	0.0	0.2	1.6	1.6	0.0	b.d.l	0.5	0.1
Al <sub>2</sub> O <sub>3</sub>	27.6	23.8	13.8	18.3	22.0	33.3	22.6	14.9
FeO	0.0	14.1	5.1	5.8	0.0	0.9	23.2	3.4
MnO	0.0	0.2	b.d.l	b.d.l	0.0	b.d.l	0.9	b.d.l
MgO	b.d.l	15.4	10.5	14.6	0.0	b.d.l	11.3	6.7
CaO	8.6	7.4	21.2	12.2	2.8	24.1	6.5	11.8
Na <sub>2</sub> O	6.6	b.d.l	2.3	2.6	10.4	b.d.l	b.d.l	7.4
K <sub>2</sub> O	0.3	b.d.l	b.d.l	2.2	0.3	b.d.l	b.d.l	b.d.l
Cr <sub>2</sub> O <sub>3</sub>	0.0	b.d.l	b.d.l	b.d.l	0.0	b.d.l	b.d.l	b.d.l
P <sub>2</sub> O <sub>5</sub>	0.0	b.d.l	b.d.l	b.d.l	n.a	n.a	n.a	n.a
SO <sub>2</sub>	b.d.l	b.d.l	b.d.l	b.d.l	n.a	n.a	n.a	n.a
Cl	0.0	b.d.l	b.d.l	0.1	n.a	n.a	n.a	n.a
BaO	0.1	b.d.l	b.d.l	b.d.l	0.1	b.d.l	n.a	n.a
Total	101.6	102.4	101.3	98.6	100.1	97.5	101.4	100.0
	An 41	Py 56	Ts 00		An 13		Py 40	Ts 03
	Ab 58	Alm 25	Di 64		Ab 86		Alm 43	Di 34
	Or 01	Grs 19	Hd 17		Or 01		Grs 17	Hd 10
			Jd 19					Jd 53

Figure	Figure 7a		Figure 7c		Figure 7d			Figure S3 a		
Mineral / Texture	analcime pools	plagioclase in matrix	analcime pools	analcime pools	analcime in vein	plagioclase in matrix	plagioclase around ky	analcime pools	analcime in matrix	plagioclase around ky
Number of analysis	7	4	7	8	7	3	1	2	1	3
SiO <sub>2</sub>	57.8	63.1	57.3	57.9	57.3	64.0	64.1	57.5	64.1	60.5
TiO <sub>2</sub>	0.0	0.0	0.0	0.0	0.0	0.0	0.0	0.0	0.0	0.0
Al <sub>2</sub> O <sub>3</sub>	23.1	23.3	22.8	22.7	22.8	22.3	22.0	22.2	22.1	25.3
FeO	0.0	0.0	0.0	0.0	0.0	0.0	0.0	0.0	0.1	0.0
MnO	0.0	0.0	0.0	0.0	0.0	0.0	0.0	0.0	0.0	0.0
MgO	0.0	0.0	0.0	0.0	0.0	0.0	0.0	0.0	0.0	0.0
CaO	0.0	4.0	0.0	0.0	0.0	3.3	3.2	0.0	3.2	5.6
Na <sub>2</sub> O	10.0	9.2	11.6	9.8	11.9	10.2	10.3	11.6	10.1	8.4
K <sub>2</sub> O	0.0	0.4	0.0	0.0	0.0	0.3	0.4	0.0	0.3	0.3
Cr <sub>2</sub> O <sub>3</sub>	n.a	0.0	n.a	n.a	n.a	0.0	0.0	n.a	0.0	0.1
P <sub>2</sub> O <sub>5</sub>	n.a	0.1	n.a	n.a	n.a	0.0	0.0	n.a	0.0	0.0
SO <sub>2</sub>	n.a	0.0	n.a	n.a	n.a	0.0	0.0	n.a	0.0	0.0
Cl	n.a	0.0	n.a	n.a	n.a	0.0	0.0	n.a	0.0	0.0
BaO	n.a	0.1	n.a	n.a	n.a	0.0	0.1	n.a	0.2	0.0
Total	91.0	100.2	91.7	90.4	92.0	100.1	100.1	91.3	100.1	100.2
		An 19				An 15	An 29		An 14,5	An 26
		Ab 79				Ab 83	Ab 70		Ab 83,5	Ab 72
		Or 02				Or 02	Or 01		Or 02	Or 02

	Pl <sub>0</sub>	Pl <sub>1</sub>	Whole rock
SiO <sub>2</sub>	57.52	64.53	49.03
TiO <sub>2</sub>	0.00	0.00	0.18
Al <sub>2</sub> O <sub>3</sub>	27.23	22.05	22.96
FeO	0.00	0.00	6.27
MgO	0.00	0.00	7.66
CaO	8.50	2.76	10.27
Na <sub>2</sub> O	6.55	10.40	3.22
K <sub>2</sub> O	0.20	0.26	0.40



**Figure S1. Transect T2 through the eclogitic finger.** BSE image (a) and photomicrograph in unanalyzed polarized light (b), see location in Figure 1d. Red zones in (b): corona structures that define the granulitic foliation. Orange arrows: plagioclase-plagioclase grain boundaries in low transformed areas. White arrows: analcime-kyanite decorated grain boundaries. Red arrows: fractures inside garnet.



**Figure S2.** Orientation map of a plagioclase grain plotted with a colormap (inset) corresponding to the angle between X direction, here defined as parallel to the [100] direction, and the thin section plane. Y perpendicular to the plane (010). Pink: untwinned, yellow: twinned. Inset also shows corresponding focal mechanism-like «beach-ball»

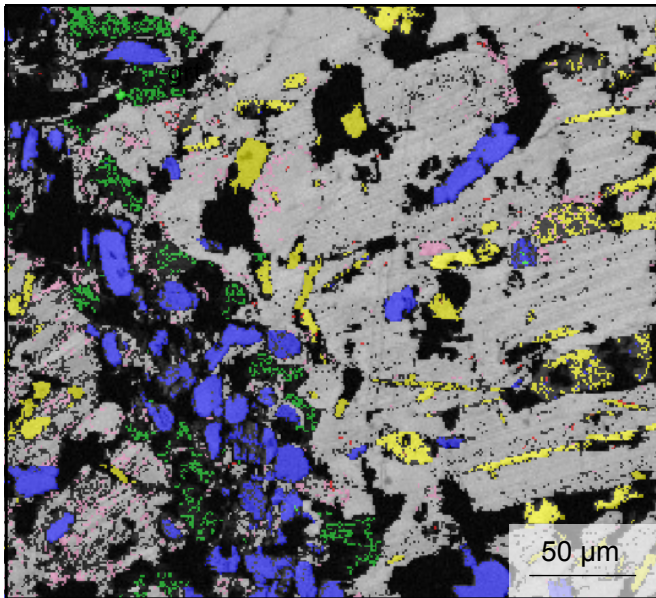


**Figure S3. EBSD image of an analcime-kyanite bearing grain boundary.** In this map, analcime has been indexed.

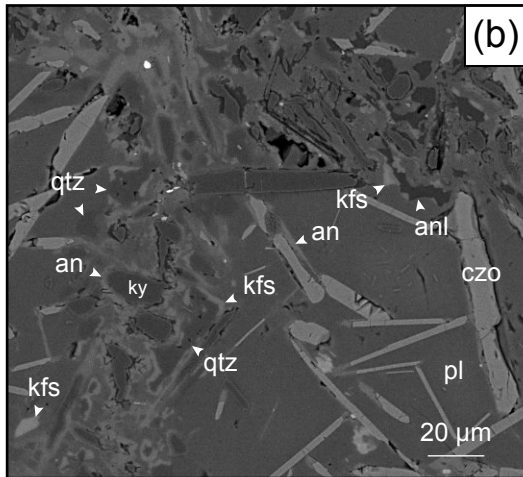
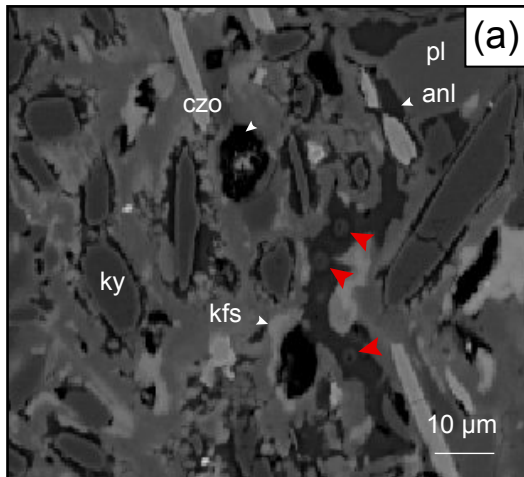


**Figure S4. Textures of analcime-bearing grain boundaries** (a) BSE image of an analcime bearing plagioclase-plagioclase grain boundary. Red arrows: holes created by the electron beam in an analcime pool. (b) BSE image of the intersection of two analcime-kyanite bearing plagioclase grain boundaries.

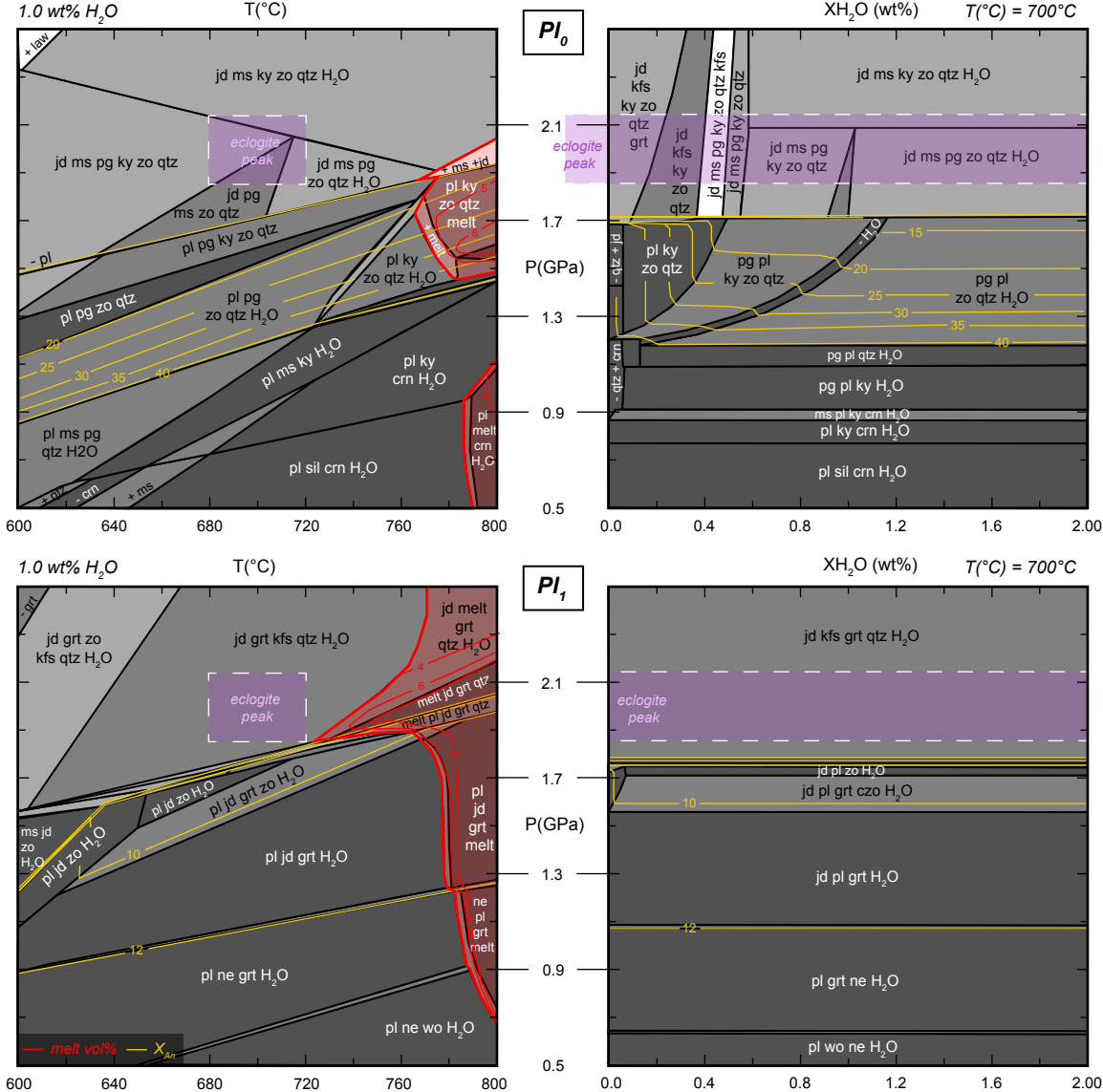


**Figure S5.**  $P$ - $T$  pseudosections at  $X_{H_2O} = 1\text{ wt\%}$  (left) and  $P$ - $X_{H_2O}$  pseudosections at  $T = 700^\circ\text{C}$  (right) for the initial plagioclase composition ( $PI_0$ ) and the partially reacted plagioclase composition ( $PI_1$ ), as indicated in Table 3. Calculations have been performed using the melt solution model of Holland & Powell 2001, see Method section for details. Zones where melt is predicted are highlighted in red. Melt modes (in volume %) are indicated by the red lines, and anorthite content in plagioclase by the yellow lines.

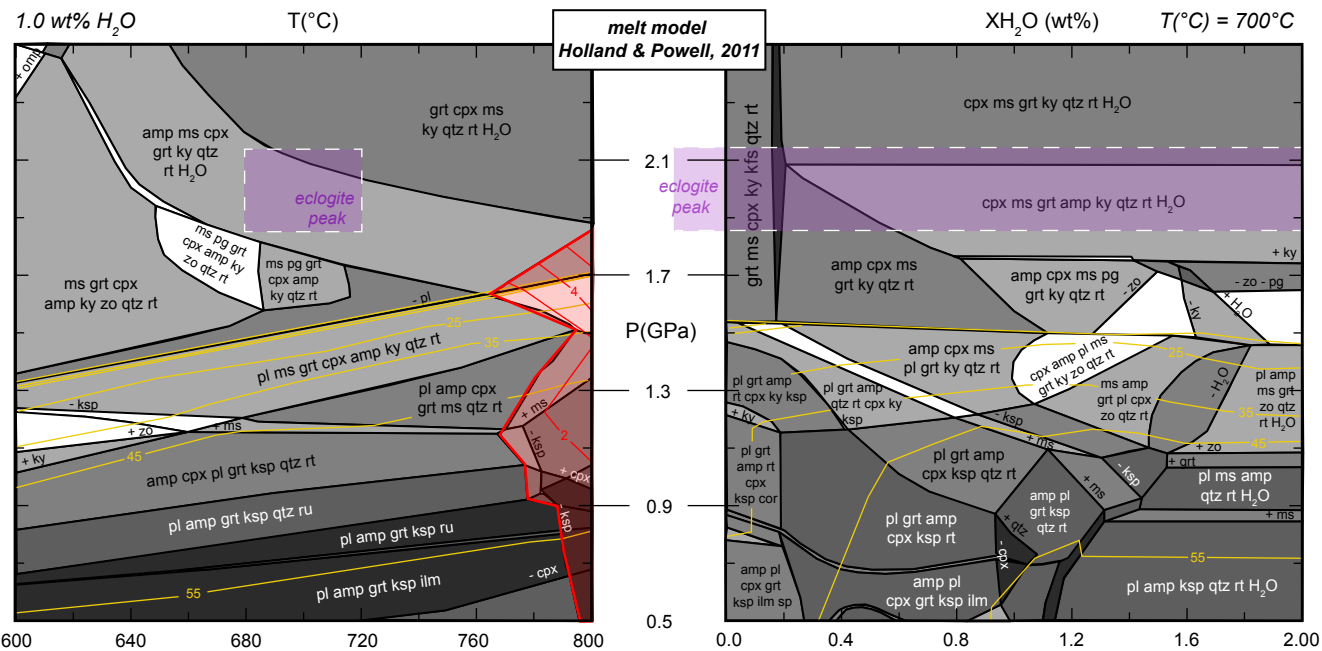
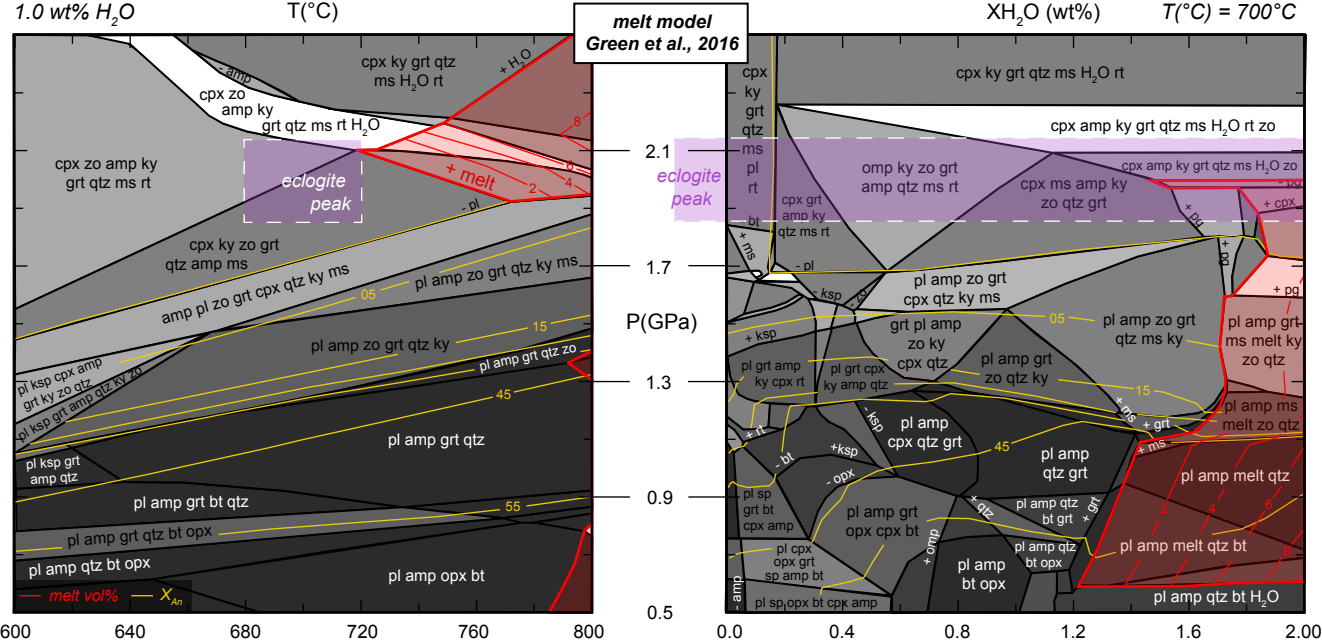


**Figure S6.** *P-T* pseudosections at  $X_{H_2O} = 1$  wt % (left) and *P-X<sub>H2O</sub>* pseudosections at  $T = 700^\circ\text{C}$  (right) for the whole rock composition of the studied sample, as indicated in Table 3. Calculations have been performed using the melt solution model of Green et al. (2016) (top) and Holland & Powell (2001) (bottom), see Method section for details. Zones where melt is predicted are highlighted in red. Melt modes (in volume %) are indicated by the red lines, and anorthite content in plagioclase by the yellow lines.